Reduced Dimer Production in Solar-Simulator-Pumped Continuous Wave Iodine Lasers Based on Model Simulations and Scaling and Pumping Studies

Robert C. Costen
Langley Research Center • Hampton, Virginia

John H. Heinbockel
Old Dominion University • Norfolk, Virginia

Gilda A. Miner and Willard E. Meador, Jr.
Langley Research Center • Hampton, Virginia

Bagher M. Tabibi
Hampton University • Hampton, Virginia

Ja H. Lee and Michael D. Williams
Langley Research Center • Hampton, Virginia

March 1995

Contents

Abstract

A numerical rate equation model for a continuous wave iodine laser with longitudinally flowing gaseous lasant is validated by approximating two experiments that compare the perfluoroalkyl iodine lasants n-C_3F_7I and t-C_4F_9I. The salient feature of the simulations is that the production rate of the dimer $(C_4F_9)_2$ is reduced by one order of magnitude relative to the dimer $(C_3F_7)_2$. The model is then used to investigate the kinetic effects of this reduced dimer production—especially how it improves output power. Related parametric and scaling studies are also presented. When dimer production is reduced, more monomer radicals (t-C_4F_9) are available to combine with iodine ions, thus enhancing depletion of the laser lower level and reducing buildup of the principal quencher, molecular iodine. Fewer iodine molecules result in fewer downward transitions from quenching and more transitions from stimulated emission of lasing photons. Enhanced depletion of the lower level reduces the absorption of lasing photons. The combined result is more lasing photons and proportionally increased output power.

Q	lasant heating from pump, $W \cdot m^{-3}$		ν_p	pump frequency, Hz
q_i	quenching rate coefficient, $cm^3 \cdot sec^{-1}$		ξ_1	photodissociation rate of [RI], sec^{-1}
R	gas constant, $8.314 \; J \cdot mol^{-1} \cdot K^{-1}$		ξ_2	photodissociation rate of [I_2], sec^{-1}

$$R^* \qquad = \frac{R}{M \times 10^{-3}} \; J \cdot kg^{-1} \cdot K^{-1}$$

R radical $n\text{-}C_3F_7$, $t\text{-}C_4F_9$, or $f\text{-}C_3F_7$

R_a reflectivity of highly reflecting mirror, 1.0

R_b reflectivity of output mirror, 0.75

r radial coordinate in cylindrical frame, m

r_N normalized radial coordinate, $\dfrac{r}{r_t}$

r_t inner radius of laser tube, m

S distance along inner perimeter of laser tube, m

s arc length, m

SC solar constant, $1.35 \; kW \cdot m^{-2}$

T lasant temperature, K

w lasant flow speed

Z axial distance downstream of pump entrance

Z_{G+} axial distance on which inversion density $[I^*] - [I]/2 > 0$, positive gain length, cm

Z_L active length of laser tube, 33 cm

Z_p length of pump, 15 cm

z normalized axial distance downstream of pump entrance, $\dfrac{Z}{Z_L}$

z_{G+} normalized positive gain length, $\dfrac{Z_{G+}}{Z_L}$

z_p normalized pump length, $\dfrac{Z_p}{Z_L} = 0.45$

α constant for C_v (eq. (26)), $J \cdot mol^{-1} \cdot K^{-1}$

β constant for C_v (eq. (26)), K^{-1}

γ distance along light ray, m

δ absorption length for pumping photons, m

η density of lasant gas, $kg \cdot m^{-3}$

θ angle, rad

ν_L frequency of laser beam, Hz

ρ number density of lasing photons, $\rho_+ + \rho_-$, photons $\cdot cm^{-3}$

$\rho_\pm$ number density of lasing photons moving along Z-axis, photons $\cdot cm^{-3}$

ρ_p number density of pumping photons, photons $\cdot cm^{-3}$

ρ_{pN} normalized pumping photon density

σ cross section for laser-beam absorption and stimulated emission, cm^2

ψ angle, rad

[ ] number density, particles $\cdot cm^{-3}$

$\langle \; \rangle$ average over cross section of laser tube

Subscript:

0 value at $Z = 0$

Model Description

Laser Geometry

The CW laser used in references 14 and 15 is shown schematically in figure 1. The Z-axis of the 1-D mathematical model is parallel to the optical axis of the laser cavity and points in the direction of the lasant flow. The origin is located where the lasant enters the elliptical pump chamber. Upstream of this point, the lasant is undissociated and does not interact with the laser beam, provided the lasant is free of absorbing or scattering impurities. The pumping region spans the distance $0 \le Z \le Z_p$, where $Z_p = 15$ cm. We assume that the incident pumping radiation at the laser tube is axisymmetric. Measurements of the actual incident pumping radiation are given in appendix D. Downstream of the pump, the lasant has a nonzero inversion density and continues to interact with the laser beam until the lasant is withdrawn at the end of the tube Z_L, where $Z = Z_L = 33$ cm. In the computation, the active length of the laser tube $(0 \le Z \le Z_L)$ is normalized to unity $(0 \le z \le 1)$, and the pump spans the normalized distance $0 \le z \le z_p$, where $z_p = 0.45$.

Photochemical Reactions

The kinetic reactions included in the laser model are as follows.

2

Introduction

A solar power station advantageously placed in space could beam power to other spacecraft and to planetary surfaces, including the surface of the Earth, as discussed in references 1–3. Experiments related to this concept include tests of solar-simulator-pumped iodine lasers, as discussed in references 4–7. These experiments are supported by modeling efforts reported in references 8–13. An important finding is that the gaseous perfluoroalkyl iodine lasants n-C_3F_7I and t-C_4F_9I have markedly different production rates for the dimers $(C_3F_7)_2$ and $(C_4F_9)_2$. Our modeling effort is devoted principally to understanding the effects of this differing dimer production on laser performance.

Lee (ref. 14) and Lee et al. (ref. 15) present two experimental comparisons of the lasants n-C_3F_7I and t-C_4F_9I when flowed longitudinally in a continuous wave (CW) laser. Laser output power is measured in the first comparison as the lasant flow speed is varied and in the second comparison as the intensity of the solar-simulator pump is varied. In both comparisons, the output power P_{out} for t-C_4F_9I is found to be about three times greater than that for n-C_3F_7I. This increase in P_{out} is not explained by an increased utilization of the pump spectrum. For the solar simulator used, the pump spectrum utilization is only 20 percent greater for t-C_4F_9I than for n-C_3F_7I.

The dimer density is represented by $[R_2]$, where R represents either of the perfluoroalkyl radicals n-C_3F_7 or t-C_4F_9 and brackets denote the number density. Ershov, Zalesskǐi, and Sokolov (ref. 16) have shown experimentally that the rate of $[R_2]$ production is much less for t-C_4F_9I than for n-C_3F_7I, although a numerical value for the ratio of these production rates is not given. Lee (ref. 14) notes that the reduced $[R_2]$ production increases t-C_4F_9I recyclability. He also speculates that the reduced $[R_2]$ production for t-C_4F_9I would make more monomer radicals $[R]$ available to combine with iodine atoms $[I]$. Consequently, more of the laser lower level $[I]$ would be depleted and less $[I_2]$, the principal quencher of excited iodine $[I^*]$, would be formed. This reduction of $[I_2]$ would also reduce the lasant flow speed.

Our purpose is to examine these speculations and especially to determine the kinetic effects of reduced $[R_2]$ production on P_{out}. Our approach is to use a one-dimensional (1-D) numerical rate equation model. This model is described in the next section. The model is tuned by using the data given in references 14 and 15; a discussion of that process follows the model description. Thereafter, general properties of the tuned model and its solutions are given. The solutions indicate that the experimental power curves obtained in references 14 and 15 could be improved by optimizing the lasant flow speed w

so that molecular iodine does not build up within the pump region of the laser. This optimization is based on parametric and scaling studies that are presented in appendixes A–D. The flow speed optimization is modeled in the section "Diagnostic Plots," and the n-C_3F_7I and t-C_4F_9I lasants are again compared. A fictitious lasant (identical to n-C_3F_7I except for a reduced $[R_2]$ production rate) is modeled in the section, "Optimization of Laser Performance." The purpose is to isolate the kinetic effects of reduced $[R_2]$ production. Concluding remarks are given next and the appendixes follow.

Symbols

B	brightness of pump lamp image, $W \cdot m^{-2} \cdot rad^{-1}$
C	carbon atom
C_1, C_2	constants of integration
C_p	specific heat at constant pressure, $J \cdot mol^{-1} \cdot K^{-1}$
C_p^*	$\dfrac{C_p}{M \times 10^{-3}}, J \cdot kg^{-1} \cdot K^{-1}$
C_v	specific heat at constant volume, $J \cdot mol^{-1} \cdot K^{-1}$
c	speed of light in vacuum
c_i	three-body, reaction-rate coefficients, $cm^6 \cdot sec^{-1}$
e	energy density of pump radiation, $J \cdot m^{-3}$
F	incident flux of pump radiation, W/m^2
F	fluorine atom
f-C_3F_7I	fictitious lasant identical to n-C_3F_7I, except that k_3 and k_4 are reduced by factor of 0.1
h	Planck's constant, $6.626 \times 10^{-34} J \cdot sec$
I	iodine atom
I_p	intensity of pump radiation, SC
I^*	iodine atom in excited state
I_2	molecular iodine
k_i	two-body reaction rate coefficients, $cm^3 \cdot sec^{-1}$
M	molecular weight, $g \cdot mol^{-1}$
P_{out}	laser output power, W
p	lasant pressure, Pa
p_{out}	laser output power density, $W \cdot cm^{-2}$

$$\frac{d}{dZ}(w\,[I^*]) = \xi_1\,[RI] + 0.51\,\xi_2\,[I_2] - k_1\,[R]\,[I^*]$$
$$- q_2\,[I_2]\,[I^*] - c\sigma\rho\left([I^*] - \frac{1}{2}[I]\right)$$
$$- q_3\,[R]\,[I^*] - q_4\,[R_2]\,[I^*]$$
$$- q_5\,[I^*]\,[I] - k_7\,[RI]\,[I^*]$$
$$- c_1\,[RI]\,[I^*]\,[I] - q_1\,[RI]\,[I^*] \qquad (6e)$$

$$\frac{d}{dZ}(w\,[I]) = 1.49\,\xi_2\,[I_2] + q_1\,[RI]\,[I^*]$$
$$+ q_2\,[I_2]\,[I^*] - 2c_5\,[I]^2\,[R_2]$$
$$- k_8\,[I]\,[RI] + k_9\,[RI]$$
$$+ c\sigma\rho\left([I^*] - \frac{1}{2}[I]\right)$$
$$- c_1\,[RI]\,[I^*]\,[I] - 2c_2\,[RI]\,[I]^2$$
$$+ 2c_4\,[I_2]\,[I]^2 - k_2\,[R]\,[I]$$
$$+ k_4\,[RI]\,[R] + q_3\,[I^*]\,[R]$$
$$+ q_4\,[I^*]\,[R_2] + q_5\,[I^*]\,[I]$$
$$+ k_5\,[R]\,[I_2] \qquad (6f)$$

where c is the speed of light in vacuum and ρ is the number density of lasing photons.

The latter density is given by

$$\rho = \rho_+ + \rho_- \qquad (7)$$

where the symbols $+$ and $-$ indicate the direction of photon motion along the Z-axis. For steady-state CW operation, these photon densities satisfy the equations

$$\frac{d\rho_+}{dZ} = \rho_+\sigma\left([I^*] - \frac{1}{2}[I]\right) \qquad (8a)$$

$$\frac{d\rho_-}{dZ} = -\rho_-\sigma\left([I^*] - \frac{1}{2}[I]\right) \qquad (8b)$$

and the boundary condition at $Z = 0$

$$\rho_+(0) = R_a\rho_-(0) \qquad (9a)$$

At $Z = Z_L$

$$\rho_-(Z_L) = R_b\rho_+(Z_L) \qquad (9b)$$

where R_a and R_b are the mirror reflectivities at $Z = 0$ and $Z = Z_L$, respectively. The quantity $\rho_-(Z)$ may be

eliminated from the formulation because equations (8a) and (8b) are satisfied by

$$\rho_+(Z)\,\rho_-(Z) = \text{Constant} \qquad (10)$$

The boundary conditions (eqs. (9a) and (9b)) then give

$$\rho_-(Z) = \frac{\rho_+(0)^2}{R_a\rho_+(Z)} \qquad (11a)$$

and from equation (7)

$$\rho(Z) = \rho_+(Z) + \frac{\rho_+(0)^2}{R_a\rho_+(Z)} \qquad (11b)$$

The boundary conditions (eqs. (9a) and (9b)) also reduce to

$$\rho_+(Z_L) = \rho_+(0)\,(R_aR_b)^{-1/2} \qquad (12)$$

The formulation is now complete in terms of $\rho_+(Z)$, and $\rho_-(Z)$ is determined from equation (11a). The output power density p_{out} in $W \cdot cm^{-2}$ is given by

$$P_{out} = \rho_+(Z_L)\,(1-R_b)\,ch\nu_L \qquad (13)$$

Compressible Fluid Dynamics

Part of the incident pump power is dissipated by heat. The resulting dependence on Z (m) of temperature T (K), pressure p (Pa), and speed w (m $\cdot$ sec^{-1}) is determined approximately from the 1-D, steady-state fluid dynamic equations for an inviscid, nonconducting gas (ref. 22) as follows.

Continuity equation. Under all these conditions the continuity equation becomes

$$\frac{d}{dZ}\eta w = 0 \qquad (14)$$

where η is the density (kg $\cdot$ m^{-3}). Hence,

$$\eta = \frac{C_1}{w} \qquad (15)$$
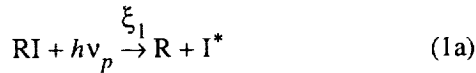
where the constant C_1 is given by

$$C_1 = \eta_0 w_0 \qquad (16)$$

where η_0 is the density and w_0 is the speed at $Z = 0$.
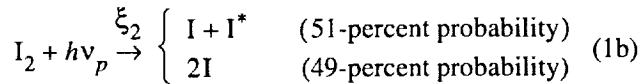
Momentum equation. The corresponding momentum equation is

$$w\frac{dw}{dZ} = -\frac{1}{\eta}\frac{dp}{dZ} \qquad (17a)$$

4

Photodissociation reactions. The parent molecule RI is irradiated in the pump region, and the following reaction occurs:

$$RI + h\nu_p \xrightarrow{\xi_1} R + I^* \tag{1a}$$

where h is Planck's constant, $h\nu_p$ is the energy of pumping photons, ξ_1 is the photodissociation rate of RI, and $I^* = {}^2P_{1/2}$, which is the laser upper level. A sequence of reactions produces I_2, which can also be photodissociated in the pump according to the reactions
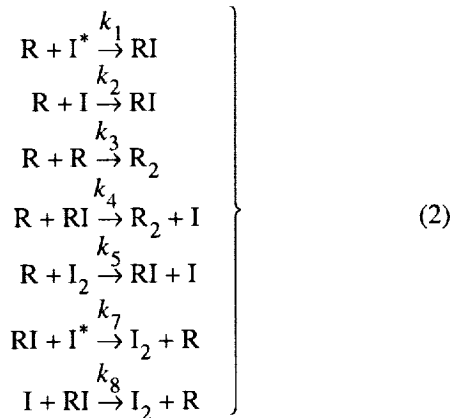
$$I_2 + h\nu_p \xrightarrow{\xi_2} \begin{cases} I + I^* & \text{(51-percent probability)} \\ 2I & \text{(49-percent probability)} \end{cases} \tag{1b}$$

where ξ_2 is the photodissociation rate of I_2, and $I = {}^2P_{3/2}$, which is the laser lower level. Photodissociation rates for ξ_1 and ξ_2 are listed in table I with other laser rate coefficients. Data in this table were obtained from references 17–21.

Absorption and stimulated emission reactions. Photons in the laser beam can be absorbed by I atoms or undergo stimulated emission by excited I^* atoms according to the reactions
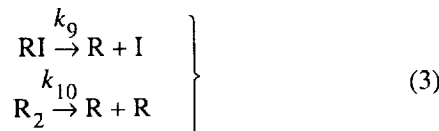
$$I^* + h\nu_L \xrightarrow{\sigma} I + 2h\nu_L \tag{1c}$$
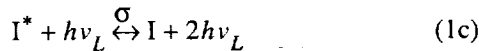
where $h\nu_L$ is the energy of the lasing photons and σ is the cross section for absorption and stimulated emission.

Two-body reactions.

$$\left. \begin{array}{l} R + I^* \xrightarrow{k_1} RI \\ R + I \xrightarrow{k_2} RI \\ R + R \xrightarrow{k_3} R_2 \\ R + RI \xrightarrow{k_4} R_2 + I \\ R + I_2 \xrightarrow{k_5} RI + I \\ RI + I^* \xrightarrow{k_7} I_2 + R \\ I + RI \xrightarrow{k_8} I_2 + R \end{array} \right\} \tag{2}$$
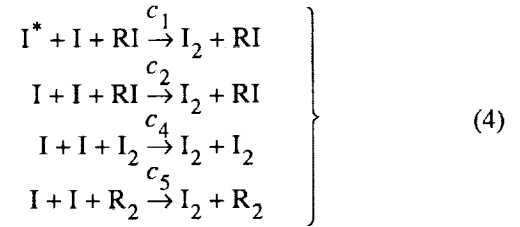
where k_i are two-body reaction-rate coefficients.

Pyrolysis. The lasant RI and dimer R_2 can also undergo thermal dissociation, especially at high temperatures. Thus,
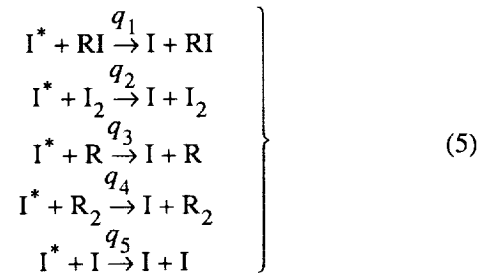
$$\left. \begin{array}{l} RI \xrightarrow{k_9} R + I \\ R_2 \xrightarrow{k_{10}} R + R \end{array} \right\} \tag{3}$$

Three-body reactions.

$$\left. \begin{array}{l} I^* + I + RI \xrightarrow{c_1} I_2 + RI \\ I + I + RI \xrightarrow{c_2} I_2 + RI \\ I + I + I_2 \xrightarrow{c_4} I_2 + I_2 \\ I + I + R_2 \xrightarrow{c_5} I_2 + R_2 \end{array} \right\} \tag{4}$$

where c_i are the three-body reaction-rate coefficients.

Quenching reactions. The following reactions quench the excited state of iodine atoms:

$$\left. \begin{array}{l} I^* + RI \xrightarrow{q_1} I + RI \\ I^* + I_2 \xrightarrow{q_2} I + I_2 \\ I^* + R \xrightarrow{q_3} I + R \\ I^* + R_2 \xrightarrow{q_4} I + R_2 \\ I^* + I \xrightarrow{q_5} I + I \end{array} \right\} \tag{5}$$

where q_i are the quenching reaction-rate coefficients.

Rate Equations

For steady-state CW operation, the 1-D rate equations are purely functions of Z as shown:

$$\begin{aligned} \frac{d}{dZ}(w[RI]) = {} & k_1[R][I^*] + k_2[R][I] \\ & + k_5[R][I_2] - k_7[I^*][RI] \\ & - k_4[R][RI] - \xi_1[RI] \\ & - k_8[I][RI] - k_9[RI] \end{aligned} \tag{6a}$$

$$\begin{aligned} \frac{d}{dZ}(w[R]) = {} & \xi_1[RI] - k_1[R][I^*] - k_2[R][I] \\ & - 2k_3[R]^2 - k_4[RI][R] \\ & - k_5[R][I_2] + k_7[RI][I^*] \\ & + k_8[I][RI] + k_9[RI] \\ & + 2k_{10}[R_2] \end{aligned} \tag{6b}$$

$$\frac{d}{dZ}(w[R_2]) = k_3[R]^2 + k_4[RI][R] - k_{10}[R_2] \tag{6c}$$

$$\begin{aligned} \frac{d}{dZ}(w[I_2]) = {} & c_1[RI][I^*][I] + c_2[RI][I]^2 \\ & + c_4[I_2][I]^2 - \xi_2[I_2] \\ & + k_7[RI][I^*] - k_5[R][I_2] \\ & + c_5[I]^2[R_2] + k_8[RI][I] \end{aligned} \tag{6d}$$

3

experimental conditions with these most favorable rate coefficients). Therefore, some adjustment of the rate coefficients was necessary for the theoretical study. Most rate coefficients are not measured directly but are inferred semiempirically through a combination of measurements and models. Thus, uncertainties in published values of rate coefficients depend not only on measurement uncertainties but also on model uncertainties. The latter uncertainties often are not evaluated.

Wishing to depart from the published values as little as possible, we performed a sensitivity study with the model. This study showed that under the given experimental conditions, the model was most sensitive to k_2, k_3, k_5, and q_2 and the output power was increased by increasing k_2 and k_5 and by decreasing k_3 and q_2. Accordingly, we multiplied k_2 and k_5 and also the pump photodissociation rates ξ_1 and ξ_2 by a factor of 2.55 and divided k_3 and q_2 by the same factor to achieve lasing and obtain the $n1$-model curve of figure 2(a). These adjusted values for n-C_3F_7I are listed in table I, where temperature dependence is included where known.

The $t1$-model curve of figure 2(a) was obtained next by using the t-C_4F_9I data given in table II(a) and the corresponding rate coefficients given in table I. As shown in table I, the principal difference assumed for t-C_4F_9I is that the production rate of the dimer [R_2] is reduced by a factor of 0.1 (reactions k_3 and k_4). The other rate coefficents and parameters are taken to be the same as those for n-C_3F_7I, except for M, α, β, and ξ_1. Various factors for reduced [R_2] production were also tried, but the factor 0.1 gave the best match, subject to the values assumed for the other rate coefficients of t-C_4F_9I.

We had originally found that the $n2$- and $t2$-model curves almost overlapped. Recalling that chemical analysis of the n-lasant had revealed a 20-percent dimer impurity, as shown in appendix A, we incorporated this feature into the model. This change succeeded in increasing somewhat the vertical separation of the theoretical curves in figure 2(b) without much affecting those in figure 2(a). Chemical analysis of the t-C_4F_9I lasant (appendix A) indicated an even higher amount of an unknown impurity; however, a 20-percent dimer contaminant for both n-C_3F_7I and t-C_4F_9I gave the best match in figure 2. This adjustment completed our tuning of the model.

Diagnostic Plots

Besides P_{out}, the laser model computes and plots the following densities as functions of z: the parent molecule [RI], the monomer [R], the dimer [R_2], molecular iodine [I_2], excited iodine [I^*], ground-state iodine [I], the inversion density [I^*] – [I]/2, and the lasing photon densities ρ_+ and ρ_-. Also computed and plotted are T, η, p, and w. The plots of these computed quantities (diagnostic plots)

are useful in the analysis of laser performance. Figures 3–6 present diagnostic plots for the four model curves of figure 2.

Diagnostic plots for both end points of the $n1$-model curve of figure 2(a) are shown in figure 3. These diagnostic plots show that the laser is not operating optimally. In figure 3(a), [I_2] rapidly builds up at the midpoint of the pump region (positive normalized gain length z_{G+}) and remains high downstream of this point until, at the exit of the pump region (z_p), it reaches an even higher plateau. The effects of this [I_2] buildup on [I^*], [I], and the inversion density [I^*] – [I]/2 are shown in figures 3(b)–3(d). In particular, the inversion density becomes *negative* midway through the pump region and remains so downstream of this point, although it becomes somewhat less negative at the exit of the pump region.

These modeling results are consistent with the well-known observations (ref. 19) that [I_2] is a strong quencher of [I^*] and can make the inversion density become negative. This negative inversion density results in a net absorption of lasing photons on the downstream half of the pump section, as shown by the curves for the lasing photon densities ρ_+ and ρ_- in figure 3(e). In particular, ρ_+ reaches its peak value in the middle of the pump section and thereafter decreases all the way to the output mirror at $z = 1$. Because p_{out} is proportional to ρ_+ at the output mirror, the model laser is not operating optimally. For optimal operation, ρ_+ would continue to increase until the flow exits the pump at $z = 0.45$.

Other features of this model run warrant explanation as well. Because [R] reacts much more readily with [I] than with [I^*] to form [RI] (i.e., $k_2 \gg k_1$), [R] decreases rapidly as [I] increases at the midpoint of the pump section, as shown in figure 3(f). The distribution of [R_2] is nonzero at $z = 0$ because of the 20-percent initial [R_2] contaminant, as shown in figure 3(g).

Figures 3(h)–3(k) show plots of T, w, η, and p (almost constant). These four plots are representative of all the model runs and are subsequently omitted. The moderate increases in T and w from solar-simulator-pump heating generally agree with the experiments in which a water-cooled quartz laser tube was used. (See fig. 1.)

The $t1$-model curves of figure 4 and one $n2$-model curve ($I_p = 1100$ SC) of figure 5 also show similar non-optimal laser performance. However, in the other $n2$-model curve ($I_p = 450$ SC) of figure 5 and in the $t2$-model curves of figure 6, the buildup of [I_2] occurs only downstream of the pump, which indicates optimal operation.

From equation (16), this equation may be written as

$$\frac{d}{dZ}(p + C_1 w) = 0 \qquad (17b)$$

Upon integration, we obtain

$$p = C_2 - C_1 w \qquad (18)$$

where

$$C_2 = p_0 + C_1 w_0 \qquad (19)$$

Equation of state. If the lasant is idealized as a perfect gas, the equation of state is given by

$$p = \eta R^* T \qquad (20)$$

Here, R^* $(J \cdot kg^{-1} \cdot K^{-1})$ is given by

$$R^* = \frac{R}{M \times 10^{-3}} \qquad (21)$$

where the gas constant $R = 8.314 \ J \cdot mol^{-1} \cdot K^{-1}$, and $M(g \cdot mol^{-1})$ is the molecular weight of the lasant. Solving equation (20) for T, we obtain

$$T = \frac{w}{R^*}\left(\frac{C_2}{C_1} - w\right) \qquad (22)$$

From equation (20), C_1 may also be written

$$C_1 = \frac{p_0 w_0}{R^* T_0} \qquad (23)$$

where p_0, w_0, and T_0 are all measured quantities.

Energy equation. The 1-D, steady-state energy equation for an inviscid, nonconducting perfect gas is given by

$$C_p^* \eta w \frac{dT}{dZ} - w \frac{dp}{dZ} = Q \qquad (24)$$

where C_p^* $(J \cdot kg^{-1} \cdot K^{-1})$ is the specific heat at constant pressure divided by $M \times 10^{-3}$, and Q $(W \cdot m^{-3})$ is the heat from the incident pump radiation. From equations (15), (18), and (22), this equation may be rewritten as

$$\frac{dw}{dZ} = \frac{R^* Q}{R^* C_1 w + C_p^* (C_2 - 2C_1 w)} \qquad (25)$$

Specific heats. In equation (25), C_p^* may be approximated from data in reference 22 as follows. The specific

heat at constant volume C_v $(J \cdot mol^{-1} \cdot K^{-1})$ is closely approximated by

$$C_v = \alpha \exp[\beta(T - 300)] \qquad (26)$$

where α and β are constant for each lasant as given in table I. The specific heat at constant pressure C_p in $J \cdot mol^{-1} \cdot K^{-1}$ is

$$C_p = C_v + R \qquad (27)$$

Thus, we have (in $J \cdot kg^{-1} \cdot K^{-1}$)

$$C_p^* = \frac{\alpha}{M \times 10^{-3}} \exp[\beta(T - 300)] + R^* \qquad (28)$$

and from equation (22)

$$C_p^* = \frac{\alpha}{M \times 10^{-3}} \exp\left\{\beta\left[\frac{w}{R^*}\left(\frac{C_2}{C_1} - w\right) - 300\right]\right\} + R^* \qquad (29)$$

Equation (29), which for a given lasant gas gives C_p^* as a function of w, is appropriate for substituting back into equation (25).

Numerical integration procedure. For a given heating rate $Q(Z)$ and values for the constants C_1 and C_2 (obtained by measuring p_0, T_0, and w_0 at $Z = 0$), equation (25) can be numerically integrated to give $w(Z)$. The other fluid dynamic fields, $\eta(Z)$, $p(Z)$, and $T(Z)$ follow from equations (15), (18), and (22), respectively. The flow speed $w(Z)$ appears explicitly in the rate equations (6a)–(6f). The density $\eta(Z)$ determines the parent molecule number density [RI], and $T(Z)$ enters the temperature-dependent rate coefficients.

Model Tuning

The rate equation model was tuned by matching as closely as possible the experimental curves for the lasants n-C_3F_7I and t-C_4F_9I, as given in references 14 and 15. The laboratory data for these curves are given in tables II(a) and II(b), where the original lasant flow units in standard cubic centimeters per second have been converted to meters per second. The wide range of pressure and pump I_p intensity values makes these data sets appropriate for tuning the model. The best match achieved with the model is shown in figure 2. This match, although imperfect, was obtained with difficulty as described in the discussion that follows.

The data in table II(a) for the $n1$ experiment curve of figure 2(a) gave a theoretical $P_{out} = 0$ W when used with the published rate coefficients for n-C_3F_7I that are the most favorable for lasing (i.e., the model did not even reach the threshold for lasing under the given

reduced [R_2] production are highly beneficial to efficient operation of a CW iodine laser.

Concluding Remarks

Two experiments which compare the performance of the lasants n-C_3F_7I and t-C_4F_9I can be approximated by a one-dimensional numerical rate equation model. In this model, the principal difference assumed for the lasants is that the dimer production rate for t-C_4F_9I is one order of magnitude less than for n-C_3F_7I. The model results indicated that laser output power could be increased by optimizing the lasant flow speeds so that the principal quencher, molecular iodine, does not build up within the pump region. This optimization method was based on parametric and scaling studies that are also presented. Such optimized model runs showed that t-C_4F_9I had a larger output power than n-C_3F_7I, although the power increment depended on the operating conditions.

Optimization of the flow speeds improved the basis for comparing n-C_3F_7I and t-C_4F_9I; however, the kinetic effects of reduced dimer production were still not clear because the two lasants had different molecular weights, pump spectrum utilizations, densities, and flow speed. To clarify these kinetic effects and determine how reduced dimer production results in greater output power, we also modeled a fictitious lasant f-C_3F_7I, which differed from n-C_3F_7I *only* by a reduced dimer production rate. The results of this theoretical comparison confirmed earlier speculations; that is, simply by reducing dimer production, we produce more monomer radicals (C_3F_7). These radicals then combine with iodine atoms to enhance depletion of the laser lower level and reduce the growth of the principal quencher, molecular iodine. Both of these effects tend to increase the lasing photon density and, hence, the output power.

This theoretical study also found that an order-of-magnitude decrease in the dimer production rate halves the lasant flow speed required to prevent the buildup of molecular iodine in the pump region. Also, more lasant molecules are recovered after they pass through the laser tube and less iodine molecules are produced; hence, reduced dimer production improves lasant recyclability. If other properties are equal, reduced dimer production is clearly a desirable feature for the flowing lasant in a continuous wave iodine laser.

Optimization of Laser Performance

Although we cannot prevent the buildup of $[I_2]$ downstream of the pump, we can prevent it inside the pump region, where it does the most harm, by increasing the lasant flow speed w. This effect of w—together with other factors that could be used to control the buildup of $[I_2]$—is discussed in appendix B. In this context, we take the optimal w to be the minimum flow speed for which the buildup of $[I_2]$ occurs only downstream of the pump.

We found that optimizing the theoretical power curves in figure 2 provides a better way to compare the lasants n-C_3F_7I and t-C_4F_9I. Optimizing the n1- and t1-model curves of figure 2(a) by increasing w and by eliminating the initial dimer contaminant (i.e., setting $[R_2(0)] = 0$) gives the increased P_{out} shown in figure 7. These curves show that under optimal conditions, t-C_4F_9I gives about twice as much output power as n-C_3F_7I at about half the flow speed. Figures 8 and 9 present diagnostic plots for both end points of each optimized curve shown in figure 7. These plots confirm that the buildup of $[I_2]$ occurs downstream of the pump and that the inversion density $[I^*] - [I]/2$ is positive throughout the pump region.

Similarly, optimization of the n2- and t2-model curves of figure 2(b) gives the increased P_{out} shown in figure 10. Again, t-C_4F_9I has higher output power than n-C_3F_7I, although the results are less dramatic. We conclude, for optimized flows, that t-C_4F_9I is superior to n-C_3F_7I; however, the difference in output power depends on the operating conditions.

Kinetic Analysis of Reduced Dimer Production

Although optimization of the power curves, as shown in figures 7 and 10, facilitates comparison of the lasants n-C_3F_7I and t-C_4F_9I, it does not clarify the kinetic effects of reduced dimer production because the optimized t-model curves—besides having reduced dimer production relative to the optimized n-model curves—also have different pump-spectrum utilizations, molecular weights, specific heats, densities, and flow speeds.

To analyze unambiguously the effects of reduced $[R_2]$ production, we considered a fictitious lasant f-C_3F_7I in which the *only* difference from n-C_3F_7I is reduced values for k_3 and k_4. We start with the n1-model optimal curve of figure 7. Because $[I_2]$ builds up only downstream of the pump, the same will be true for the f1-model (obtained from the n1-model optimal curve by reducing k_3 and k_4 by a factor of 0.1 without changing w or anything else).

Reduced dimer production (without other changes) gives the increased P_{out} shown by the f1-model curve

relative to the n1-model optimal curve in figure 11. Diagnostic plots for the f1-model are presented in figure 12 for comparison with the diagnostic plots for the n1-model optimum, as presented in figure 8. These diagnostic plots are supplemented by detailed plots of $[I_2]$ and [RI] for the two models in figure 13.

These diagnostic and detailed plots show clearly that a reduced $[R_2]$ production rate decreases $[R_2]$, $[I_2]$, [I], $[I^*]$, and $[I^*] - [I]/2$ in the pump region and increases [R], [RI], ρ_+, and ρ_-. The results confirm the speculations made in reference 1; that is, the decrease in $[R_2]$ and $[I_2]$ and the increase in [RI] improve lasant recyclability. The reduced $[R_2]$ production results in a greater density of monomer radicals [R] in the pump region that can combine with iodine atoms [I] and thus enhance depletion of the laser lower level and reduce the buildup of the principal quencher $[I_2]$. The lower value of $[I_2]$ increases ρ_+ and ρ_- because fewer downward transitions occur by quenching and more by the stimulated emission of lasing photons. The lower value of [I] reduces the absorption of ρ_+ and ρ_-. Hence, the reductions in $[I_2]$ and [I] both help increase the output power P_{out}, which is proportional to ρ_+ at the output mirror.

After repeating this reduced dimer analysis with the n2-model optimal curve of figure 10 and the fictitious lasant f-C_3F_7I, we obtain the increased P_{out} shown by the fictitious f2-model curve in figure 14. Figures 11 and 14 clearly show that simply by reducing the dimer production rate, we were able to increase output power, although the amount of increase depends on the operating conditions.

Although not shown, the diagnostic plots for the n2-model optimum and the f2-model are similar to those given in figures 8 and 12 for the n1-model optimum and the f1-model, respectively. The corresponding detailed plots are given in figure 15, which again shows that the reduction of $[R_2]$ production increases [RI] and decreases $[I_2]$. This second comparison reinforces the previous conclusions about the benefits of reduced $[R_2]$ production.

Finally, we investigate the speculation that reduced $[R_2]$ production allows the lasant flow speed w to be reduced. In figure 11, the values of w_0 for the fictitious f1-model are the same as for the n1-model optimum. We now optimize the f1-model by reducing w_0 to the minimum values that still prevent the buildup of $[I_2]$ inside the pump. We find that w_0 can be halved and that P_{out} is not significantly affected, as shown in figure 16. Diagnostic plots for the f1-model optimum (halved w_0) are shown in figure 17. These plots confirm that $[I_2]$ builds up only downstream of the pump. Although not shown, similar results are obtained when the fictitious f2-model of figure 14 is optimized by halving w_0. These effects of

7

Appendix A

Gas Chromatographic–Mass Spectrometric Analysis of Lasants n-C_3F_7I and t-C_4F_9I

A gas chromatographic–mass spectrometric (GCMS) device was used to examine samples of the two lasants. The findings are summarized below.

Analysis of n-C_3F_7I Sample

No significant difference was noted between the pre- and postlased n-C_3F_7I material. The analysis revealed the following compounds:

$(C_3F_7)_2$	≈ 20 percent
C_2F_5I	Trace amounts
n-C_3F_7I	≈ 80 percent
Unknown perfluorocarbon	Trace amounts
C_2F_4ClI	Trace amounts

The presence of I_2 was not detected in the GCMS analysis, even though I_2 was visually detectable in the postlased sample. Several explanations can be given for the absence of I_2 in the postlased sample: the I_2 peak was masked by either the $(C_3F_7)_2$ dimer peak or the n-C_3F_7I peak, the I_2 was trapped on the gas chromatograph column, or the I_2 concentration was so small that it was not detected on the gas chromatograph.

Analysis of t-C_4F_9I Sample

More than 20 gas chromatographic peaks were detected. Only the ethyl alcohol and t-C_4F_9I peaks could be identified. The remaining peaks contained perfluoroalkyl iodine compounds and perfluoroalkanes. The major peaks are listed below and are approximate.

Peak	Identification	Sample, percent
15	Ethyl alcohol	3
62–83	t-C_4F_9I	35
444–480	Unknown	60
1154	Unknown	2

Appendix B

Parametric and Scaling Studies

As shown in figure 3, the inversion density $[I^*] - [I]/2 > 0$ for only a fraction of the pump length Z_p. We termed this fractional distance the positive gain length Z_{G+}. We performed a parametric study to determine how Z_{G+} varies with flow speed w, number density $[RI]$, and pump intensity I_p. The result is expressed by the proportionality

$$Z_{G+} \propto \frac{w}{[RI]\sqrt{I_p}} \qquad (B1)$$

An increase in w retards the buildup of $[I_2]$, whereas an increase in $[RI]$ and I_p increases the level of photoionization and accelerates the buildup of $[I_2]$. This proportionality was used to optimize the laser model (to achieve positive gain throughout the pump region) by increasing w until $Z_{G+} = Z_p$.

A scaling study was also performed to determine how output power density p_{out} (W · cm^{-2}) scales for similar lasers—lasers that have the same ratio of positive gain length to pump length Z_{G+}/Z_p. For such similar lasers, p_{out} was found to scale according to the proportionality

$$p_{out} \propto Z_{G+} I_p [RI] \qquad (B2)$$

The output power P_{out} in W scales with the inner radius r_t of a circular cylindrical laser tube according to the proportionality

$$P_{out} \propto \langle \rho_{pN} \rangle r_t^2 \qquad (B3)$$

where $\langle \rho_{pN} \rangle$ is the normalized density of pumping photons averaged over the cross section. A derivation of $\langle \rho_{pN} \rangle$ as a function of the ratio r_t/δ, where δ is the pumping photon absorption length, is given in appendix C.

The scaling study may be summarized as follows: Two optimal CW iodine lasers are similar if the lasant flow speeds satisfy the relation

$$\frac{w_2}{w_1} = \frac{Z_{p2}}{Z_{p1}} \frac{[RI]_2}{[RI]_1} \frac{\sqrt{I_{p2}}}{\sqrt{I_{p1}}} \qquad (B4)$$

For such similar lasers, the output power P_{out} scales as

$$\frac{P_{out2}}{P_{out1}} = \frac{Z_{p2}}{Z_{p1}} \frac{[RI]_2}{[RI]_1} \frac{I_{p2}}{I_{p1}} \frac{r_{t2}^2}{r_{t1}^2} \frac{\langle \rho_{pN2} \rangle}{\langle \rho_{pN1} \rangle} \qquad (B5)$$

A plot of $\langle \rho_{pN} \rangle$ as a function of r_t/δ is given in appendix C.

Appendix C

Derivation of Average Pumping Photon Density in Absorbing Lasant With Circular Cylindrical Symmetry

This appendix provides a derivation of the quantity $\langle \rho_{pN} \rangle$ used to scale the output powers of equation (B5) in appendix B.

Two-Dimensional Relation of Incident Flux to Transmitting Surface Brightness

Assume that the laser tube and the incident pump radiation are axially symmetric and independent of Z. (Appendix D gives a discussion of how this idealization compares with theoretical and actual elliptical pump chambers.) We also assume that the optical image of the pump source fills the interior of the laser tube, as shown in figure 18, where the curved wall of the circular glass tube acts as a negative lens. Furthermore, we assume that in the absence of absorption the pump intensity is uniform and isotropic on a cross section of the pump image. Then, if we take a point on the perimeter, as shown in figure 19, the image brightness B (W · m^{-2} · rad^{-1}, interpreted as watts per meter perimeter per meter depth per radian) can be integrated to determine the incident flux of pump radiation F (W · m^{-2}):

$$F = \int_{-\pi/2}^{\pi/2} B \cos\theta \; d\theta = 2B \qquad (C1)$$

where the angle θ is in radians. A comparable 3-D relation is given in reference 23 on page 23.

Pumping Photon Density Transmitted by Surface Element

We now determine the differential pumping energy density de (J · m^{-3}) at an interior point at depth γ due to incident radiation passing through length dS of the perimeter, as shown in figure 20. Initially, assume that the laser tube is evacuated so that absorption is not a factor. Then, the power within ray $d\theta$ (W · m^{-1} depth) is given by $B \cos\theta \; dS \; d\theta$. Because this power results from photons moving at the speed of light in vacuum c, the pumping energy (J · m^{-2} (per meter depth per meter length)) within $d\theta$ is given by $(B/c) \cos\theta \; dS \; d\theta$. But

$d\theta = ds/\gamma$; hence, de (J · m^{-3}) due to the incident radiation that penetrates dS is given by

$$de = \frac{B}{c\gamma} \cos\theta \; dS \qquad (C2)$$

and the corresponding pumping photon density $d\rho_p$ (photons · m^{-3}) is given by

$$d\rho_p = \frac{B}{h\nu_p c\gamma} \cos\theta \; dS \qquad (C3)$$

For an *absorbing* lasant gas, this photon density becomes

$$d\rho_p = \frac{B}{h\nu_p c\gamma} \exp(-\gamma/\delta) \cos\theta \; dS \qquad (C4)$$

where δ is the absorption length at the pump frequency.

Total Pumping Photon Density at Interior Point Due to Axisymmetric Incident Flux

Substitution of equation (C1) into (C4) gives de at point H of figure 21 when F is transmitted through dS:

$$d\rho_p = \frac{F}{2h\nu_p c\gamma} \exp(-\gamma/\delta) \cos\theta \; dS \qquad (C5)$$

However, by introducing the angle ψ shown in figure 21 we may write

$$d\psi = \frac{\cos\theta}{\gamma} dS \qquad (C6)$$

and equation (C5) becomes

$$d\rho_p = \frac{F}{2ch\nu_p} \exp(-\gamma/\delta) \; d\psi \qquad (C7)$$

The total pumping photon density (photons · m^{-3}) at point H in an absorbing gas may then be written

$$\rho_p = \frac{F}{ch\nu_p} \int_0^\pi \exp(-\gamma/\delta) \; d\psi \qquad (C8)$$

and by the law of cosines

$$\gamma = -r\cos\psi + \sqrt{r_t^2 - r^2\sin^2\psi} \qquad (C9)$$

Hence, the pumping photon density (photons $\cdot$ m^{-3}) at radius r in an absorbing lasant is given by

$$\rho_p(r, r_t, \delta) = \frac{F}{ch\nu_p} \int_0^\pi \exp\left[\frac{1}{\delta}\left(r\cos\psi - \sqrt{r_t^2 - r^2\sin^2\psi}\right)\right]d\psi \qquad (C10)$$

The average pumping photon density over the cross section is given by

$$\langle\rho_p(r_t, \delta)\rangle = \frac{1}{\pi r_t^2} \int_0^{r_t} dr\, 2\pi r\, \rho_p(r, r_t, \delta) \qquad (C11)$$

Normalized Pumping Photon Densities

In the limit as $\delta \to \infty$, equation (C10) gives the uniform photon density for a nonabsorbing lasant as

$$\rho_p(\delta \to \infty) = \frac{\pi F}{ch\nu_p} \qquad (C12)$$

Using this quantity to normalize the photon density in equation (C10), we obtain

$$\rho_{pN}(r_N, r_t/\delta) = \frac{1}{\pi} \int_0^\pi \exp\left[\frac{r_t}{\delta}\left(r_N\cos\psi - \sqrt{1 - r_N^2\sin^2\psi}\right)\right]d\psi \qquad (C13)$$

where $r_N = r/r_t$ is the normalized radius. Plots of this normalized pumping photon density versus the normalized radius are given in figure 22 for various values of r_t/δ.

The average pumping photon density in an absorbing lasant, as given by equation (C11), can also be normalized by

$$\langle\rho_{pN}(r_t/\delta)\rangle = 2\int_0^1 dr_N r_N \rho_{pN}(r_N, r_t/\delta) \qquad (C14)$$

This normalized average pumping photon density is plotted versus r_t/δ in figure 23. This quantity is an important factor in the scaling relation (eq. (B5) from appendix B) for calculating how output power scales with the radius of the laser tube.

12

Appendix D

Theoretical and Experimental Performance of Elliptical Pump Chamber

A ray tracing for the elliptical cross section of the pump chamber used in the laser experiments is shown in figure 24(a). The rays are assumed to emanate isotopically from a line source (perpendicular to the page) at the right focus. However, the rays incident on the laser tube at the left focus are found to be nonisotropic. As shown in figure 24(a), they are more concentrated on the side toward the source. A decrease in the distance between the focii in the elliptical pump chamber makes the incident radiation at the laser tube more isotropic, as shown in figure 24(b).

An experimental polar plot of the incident pumping radiation measured inside the laser tube is shown in figure 25. Differences from the theoretical plots result from the finite size (11 mm diameter) of the pump lamp, from obstruction by the lamp start-up wire, and from imperfections in the curvature and finish of the optical surfaces, including the elliptical cylinder and the flat end plates.

References

1. Lee, Ja H. and Conway, E. J.: Power Laser Beaming and Applications in Space. *J. De Phys. IV*, vol. 1, Colloque No. 7, Dec. 1991, pp. C7-715–C7-720.

2. De Young, Russell J., ed.: *Second Beamed Space-Power Workshop*. NASA CP-3037, 1989.

3. De Young, R. J.; Walker, G. H.; Williams, M. D.; Schuster, G. L.; and Conway, E. J.: *Preliminary Design and Cost of a 1-Megawatt Solar-Pumped Iodide Laser Space-to-Space Transmission Station*. NASA TM-4002, 1987.

4. Lee, Ja H.; and Weaver, W. R.: A Solar-Simulator-Pumped Atomic Iodine Laser. *Appl. Phys. Lett.*, vol. 39, no. 2, July 15, 1981, pp. 137–139.

5. Weaver, Willard R.; and Lee, Ja H.: A Solar-Pumped Gas Laser for the Direct Conversion of Solar Energy. *J. Energy*, vol. 7, no. 6, Nov.–Dec. 1983, pp. 498–501.

6. De Young, Russell J.: Low Threshold Solar-Pumped Iodine Laser. *IEEE J. Quantum Electron.*, vol. QE-22, no. 7, July 1986, pp. 1019–1023.

7. De Young, Russell J.: Beam Profile Measurement of a Solar-Pumped Iodine Laser. *Appl. Opt.*, vol. 25, no. 21, Nov. 1, 1986, pp. 3850–3854.

8. Wilson, J. W. and Lee, J. H.: Modeling of a Solar-Pumped Iodine Laser. *Virginia J. Sci.*, vol. 31, no. 3, Fall 1980, pp. 34–38.

9. Zalesskii, V. Yu.: Iodine Laser Pumped by Solar Radiation. *Soviet J. Quantum Electron.*, vol. 13, no. 6, June 1983, pp. 701–707.

10. Wilson, John W.; Raju, S.; and Shiu, Y. J.: *Solar-Simulator-Pumped Atomic Iodine Laser Kinetics*. NASA TP-2182, 1983.

11. Wilson, John W.; Lee, Yeunggil; Weaver, Willard R.; Humes, Donald H.; and Lee, Ja H.: *Threshold Kinetics of a Solar-Simulator-Pumped Iodine Laser*. NASA TP-2241, 1984.

12. Lee, Ja H.; Wilson, John W.; Enderson, Therese; Humes, Donald H.; Weaver, Willard R.; and Tabibi, M.: Threshold Kinetic Processes for t-C_4F_9I, *Opt. Commun.*, vol. 53, no. 6, Apr. 15, 1985, pp. 367–370.

13. Hwang, In Heon; and Tabibi, Bagher M.: A Model for a Continuous-Wave Iodine Laser. *J. Appl. Phys.*, vol. 68, no. 10, Nov. 15, 1990, pp. 4983–4989.

14. Lee, Ja H.: Efficient Solar-Pumped Iodine Photodissociation Laser for Space Power Beaming. *Research and Technology 1989—Langley Research Center*, NASA TM-4150, 1990, pp. 124–125.

15. Lee, Ja H., Tabibi, Bagher M.; Humes, Donald H.; Hwang, I. H.; and Weaver, W. R.: A 10-Watt CW Photodissociation Laser With Iodo-Perfluoro-Tert-Butane. *Conference on Lasers and Electro-Optics—1989, Technical Digest Series*, Volume 11, Opt. Soc. America, pp. 188–189.

16. Ershov, L. S.; Zalesskii, V. Yu.; and Sokolov, V. N.: Laser Photolysis of Perfluoroalkyl Iodides. *Soviet J. Quantum Electron.*, vol. 8, no. 4, Apr. 1978, pp. 494–501.

17. Vinokurov, G. N.; and Zalesskii, V. Yu: Chemical Kinetics and Gasdynamics of a Q-Switched Iodine Laser With an Optically Thick Active Medium. *Soviet J. Quantum Electron.*, vol. 8, no. 10, Oct. 1978, pp. 1191–1197.

18. Brederlow, G.; Fill, E.; and Witte, K. J.: *The High-Power Iodine Laser*. Springer-Verlag, 1983.

19. Cohen, James S.; and Judd, O. P.: High-Energy Optically Pumped Iodine Laser. *J. Appl. Phys.*, vol. 55, no. 7, Apr. 1984, pp. 2659–2671.

20. Hohla, Kristian; and Kompa, Karl L.: The Photochemical Iodine Laser. *Handbook of Chemical Lasers*, R. W. F. Gross and J. F. Bott, eds., John Wiley & Sons, Inc., 1976, pp. 667–701.

21. Krug, J. K. G.; and Witte, K. J.: *Physical and Chemical Data of Substances Related to the Atomic Iodine Laser*. MPQ-61, Max-Planck-Inst. Quantenoptik, July 1982.

22. Howarth, L., ed.: *Modern Developments in Fluid Dynamics—High Speed Flow*, Volume I. Oxford Univ. Press, 1953.

23. Svelto, Orazio (David C. Hanne, transl.): *Principles of Lasers*, Third ed., Plenum Press, 1989.

Table I.   Lasant Rate Coefficients and Other Parameters

Parameter	Unit	Lasant		Reference
		$n\text{-}C_3F_7I$	$t\text{-}C_4F_9I$	
k_1	$cm^3 \cdot sec^{-1}$	1×10^{-14}	Same	17
$^*k_2$	$cm^3 \cdot sec^{-1}$	$(2.04 \pm 1.02) \times 10^{-11}$	Same	18
$^\dagger k_3$	$cm^3 \cdot sec^{-1}$	$(7.84 \pm 1.18) \times 10^{-13}$	$(7.84 \pm 1.18) \times 10^{-14}$	18
k_4	$cm^3 \cdot sec^{-1}$	3×10^{-16}	3×10^{-17}	19
$^*k_5$	$cm^3 \cdot sec^{-1}$	2.55×10^{-11}	Same	19
k_7	$cm^3 \cdot sec^{-1}$	$(3 \pm 1.5) \times 10^{-19}$	Same	19
k_8	$cm^3 \cdot sec^{-1}$	1.6×10^{-23}	Same	19
k_9	$cm^3 \cdot sec^{-1}$	$1 \times 10^{15}\exp(-2.48 \times 10^4/T)$	Same	19
k_{10}	$cm^3 \cdot sec^{-1}$	$1 \times 10^{17}\exp(-4.73 \times 10^4/T)$	Same	19
q_1	$cm^3 \cdot sec^{-1}$	$(1.7 \pm 0.2) \times 10^{-17}$	Same	18
$^\dagger q_2$	$cm^3 \cdot sec^{-1}$	$(1.49 \pm 0.10) \times 10^{-11}$ $\times \exp[-4.4 \times 10^{-3}(T-300)]$	Same	19
q_3	$cm^3 \cdot sec^{-1}$	3.7×10^{-18}	Same	19
q_4	$cm^3 \cdot sec^{-1}$	4.7×10^{-16}	Same	19
q_5	$cm^3 \cdot sec^{-1}$	1.6×10^{-14}	Same	19
c_1	$cm^6 \cdot sec^{-1}$	1.6×10^{-33}	Same	20
c_2	$cm^6 \cdot sec^{-1}$	$(5.7 \pm 1) \times 10^{-33}\exp[(1360 \pm 200)/T]$	Same	19
c_4	$cm^6 \cdot sec^{-1}$	$\text{antilog}_{10}\{-29.437 - 5.844 \log_{10}(T/300)$ $+ 2.163 [\log_{10}(T/300)]^2\}$	Same	19
c_5	$cm^6 \cdot sec^{-1}$	$(8 \pm 2) \times 10^{-33}\exp[(1310 \pm 100)/T]$	Same	19
$^\ddagger \xi_1$	sec^{-1}	$(1.2 \pm 0.4) \times 10^{-2}I_p$	$(1.44 \pm 0.48) \times 10^{-2}I_p$	
$^\ddagger \xi_2$	sec^{-1}	$(1.2 \pm 0.4) \times 10^{-1}I_p$	Same	
α	$J \cdot mol^{-1} \cdot K^{-1}$	147.23	183.26	21
β	K^{-1}	1.2×10^{-3}	1.4×10^{-3}	21
M	$g \cdot mol^{-1}$	296	346	
$[R_2(0)]$	cm^{-3}	$0.2 [RI (0)]$	Same	

*Cited value multiplied by 2.55.
†Cited value divided by 2.55.
‡Semiempirical value multiplied by 2.55.

Table II. Experimental Data for Comparison of Lasants n-C_3F_7I and t-C_4F_9I

(a) Based on reference 14 and plotted in figure 2(a);
I_p = 1000 SC; T_0 = 300 K

w_0, m·sec^{-1}	p_0, torr	P_{out}, W
Lasant n-C_3F_7I		
5.75	12.0	4.0
6.96	14.0	6.0
7.40	17.0	7.2
Lasant t-C_4F_9I		
5.07	14.0	11.1
6.45	17.0	13.8
6.72	14.5	12.5

(b) From reference 15 and plotted in figure 2(b)

I_p, SC	w_0, m·sec^{-1}	p_0, torr	P_{out}, W
Lasant n-C_3F_7I			
450	6.6	5.6	1.4
600	6.6	5.6	1.8
740	6.2	6.0	2.2
925	6.4	5.8	2.4
1100	5.8	6.4	2.7
Lasant t-C_4F_9I			
450	5.5	9.0	5.8
600	7.3	4.5	6.5
740	7.3	4.5	7.2
925	7.1	4.2	8.4
1100	7.1	4.2	9.8

16
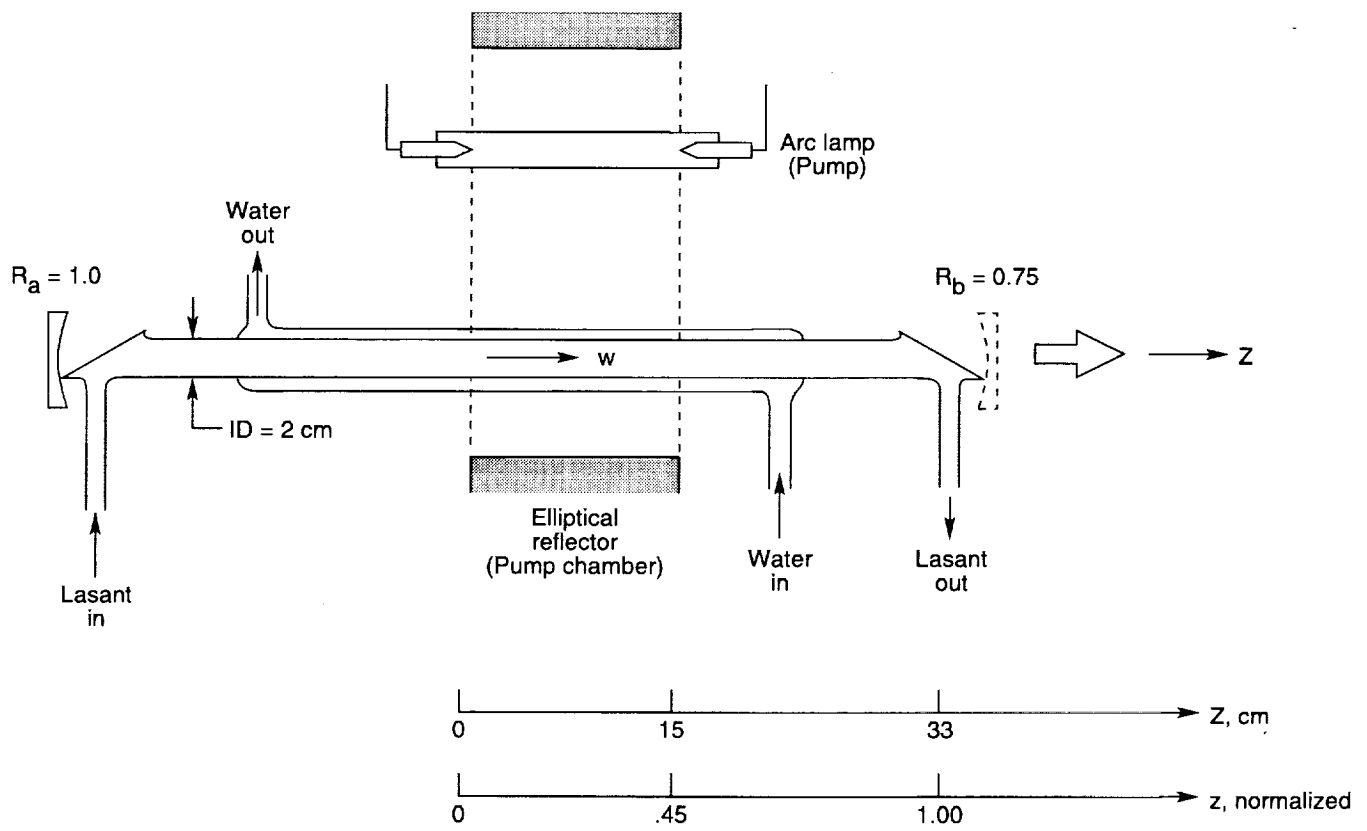
Figure 1. Laboratory schematic of CW iodine laser with longitudinally flowing lasant gas and continuous pumping by argon arc lamp.
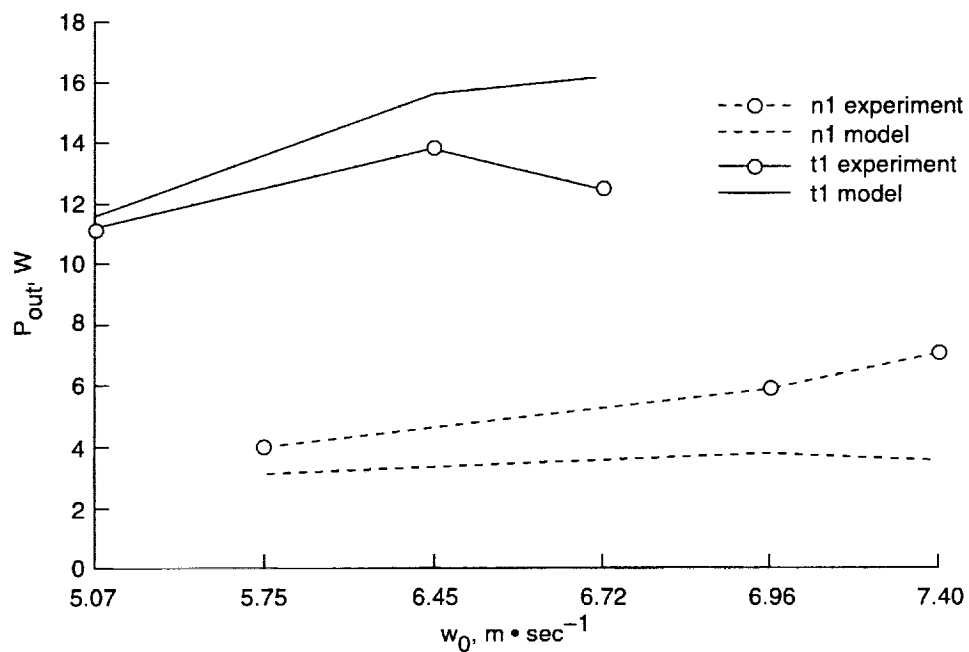
(a) Data from reference 14.
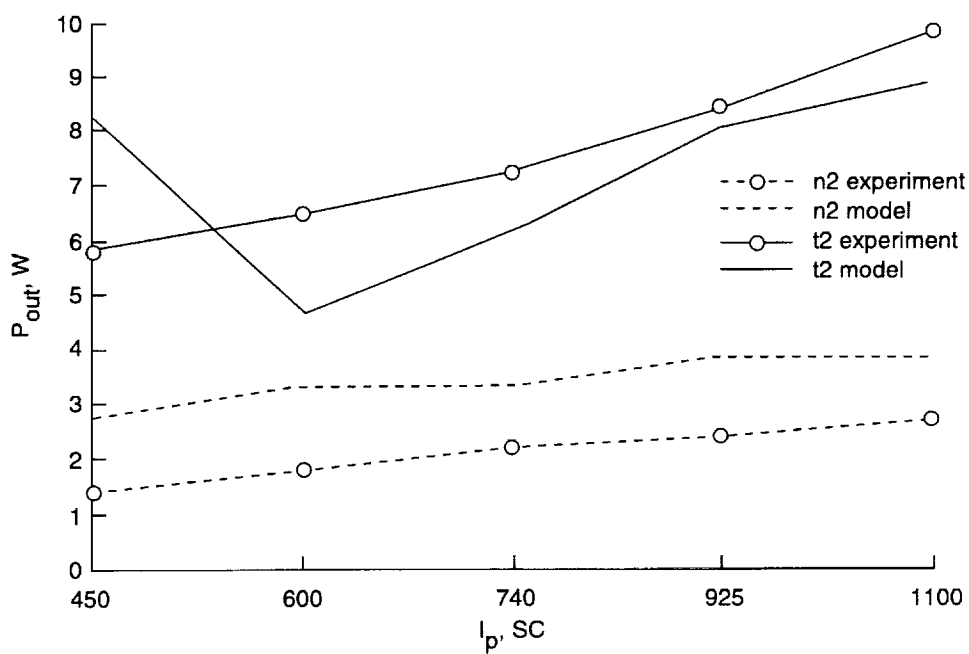
(b) Data from reference 15.

Figure 2. Experimental comparison of output power from n-C_3F_7I and t-C_4F_9I with corresponding model-tuning curves.
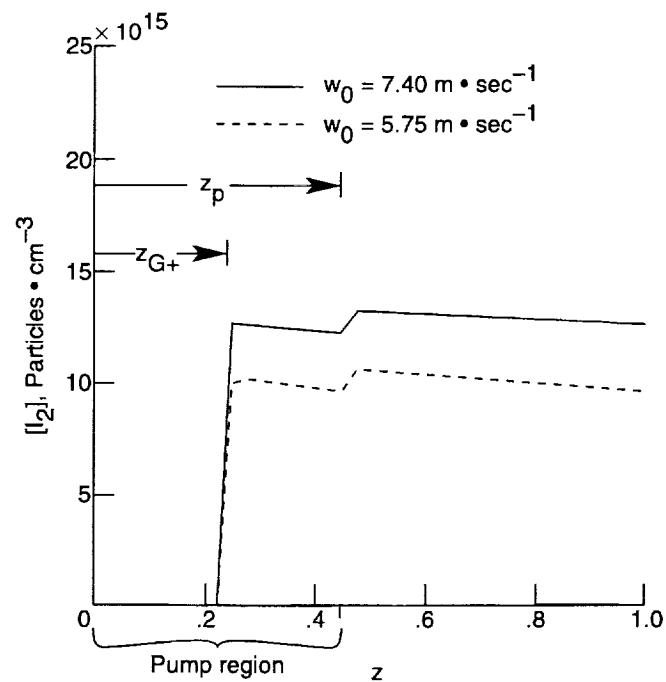
(a) Molecular iodine density [I$_2$] versus z.
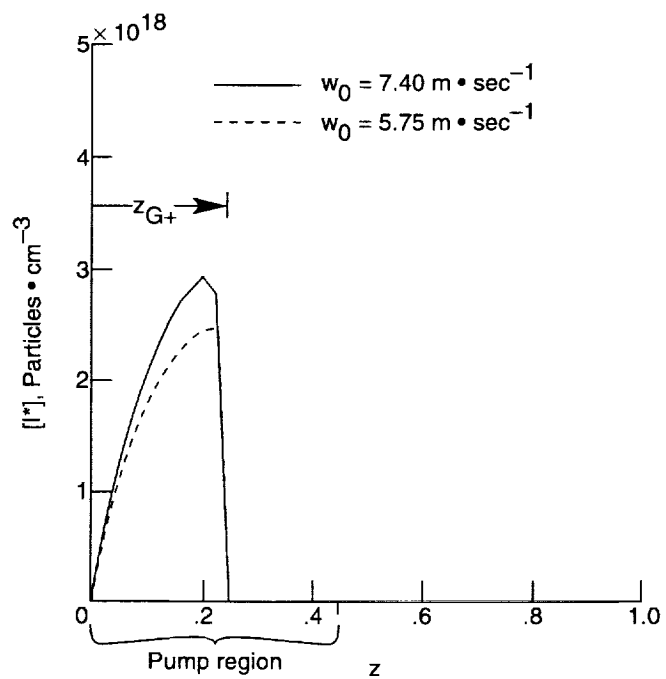
(b) Excited iodine density [I*] versus z.

Figure 3. Theoretical plots of diagnostic quantities versus z for both end points of $n1$-model curve of figure 2(a).
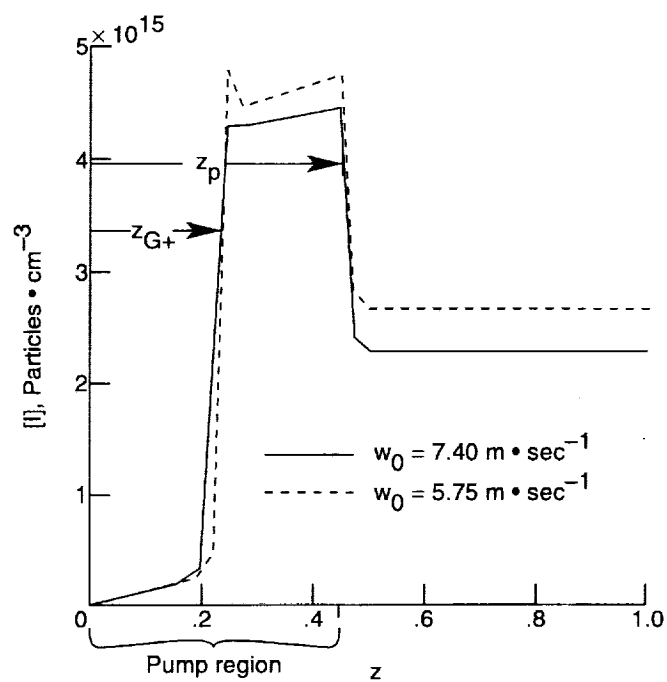
(c) Ground-state iodine density [I] versus z.
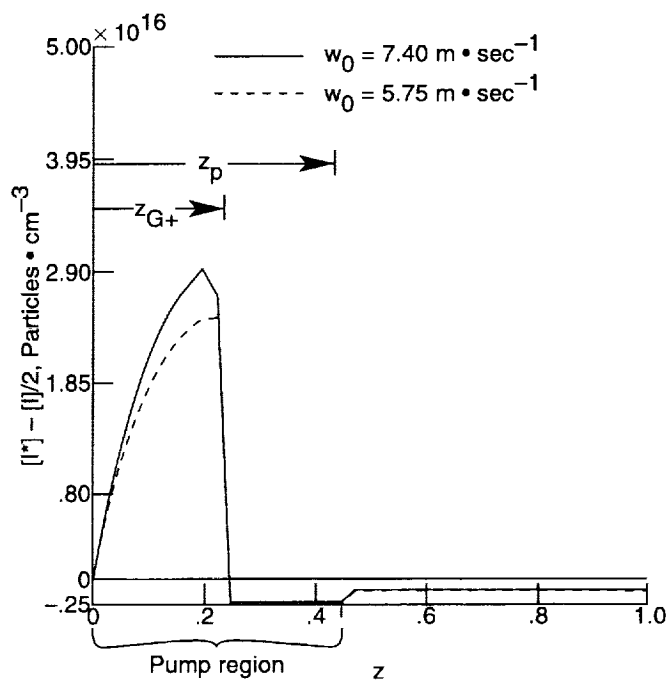
(d) Inversion density $[I^*] - [I]/2$ versus z.

Figure 3. Continued.

20
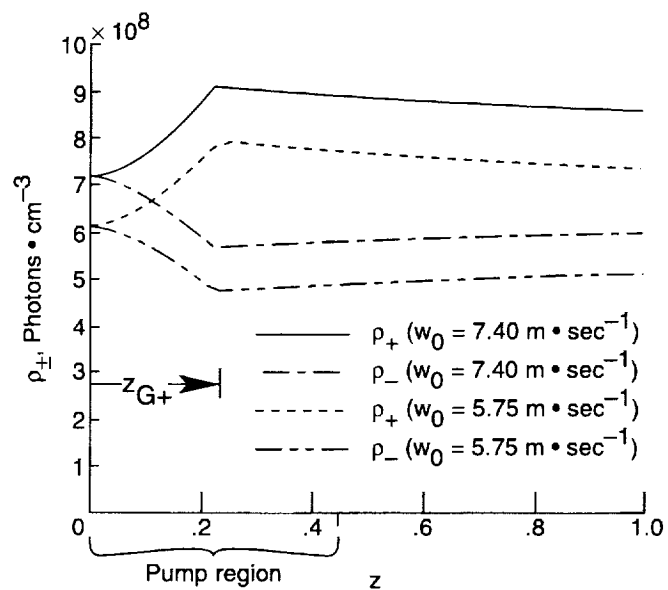
(e) Lasing photon densities ρ_+ and ρ_- versus z.
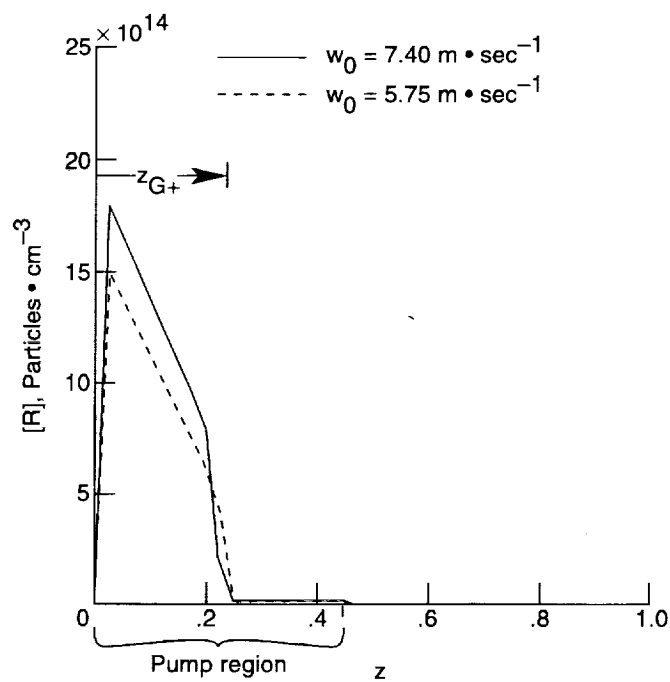
(f) Perfluoroalkyl radical density [R] versus z.

Figure 3. Continued.
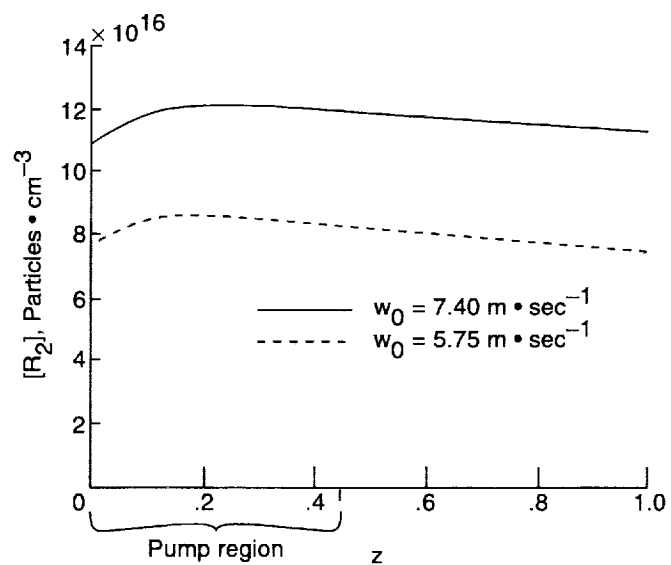
(g) Perfluoroalkyl dimer density $[R_2]$ versus z.
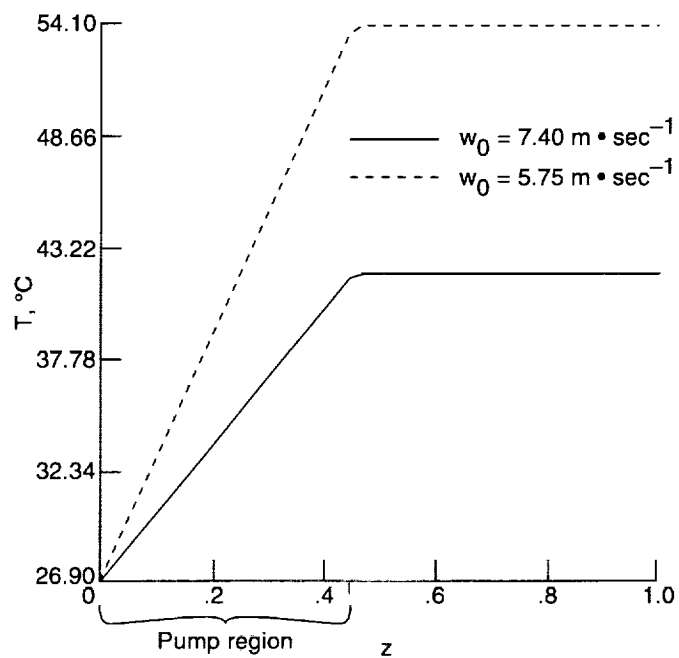
(h) Lasant temperature T versus z.

Figure 3. Continued.

22
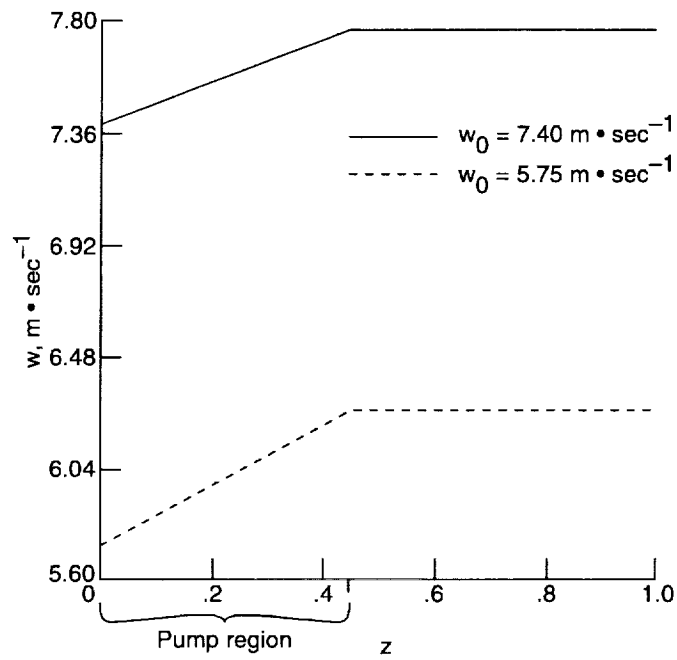
(i) Lasant flow speed w versus z.
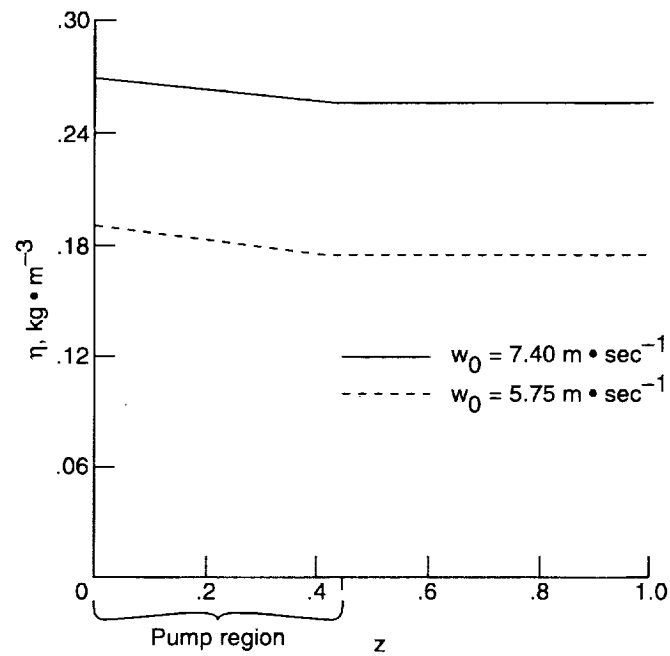
(j) Lasant density η versus z.

Figure 3. Continued.
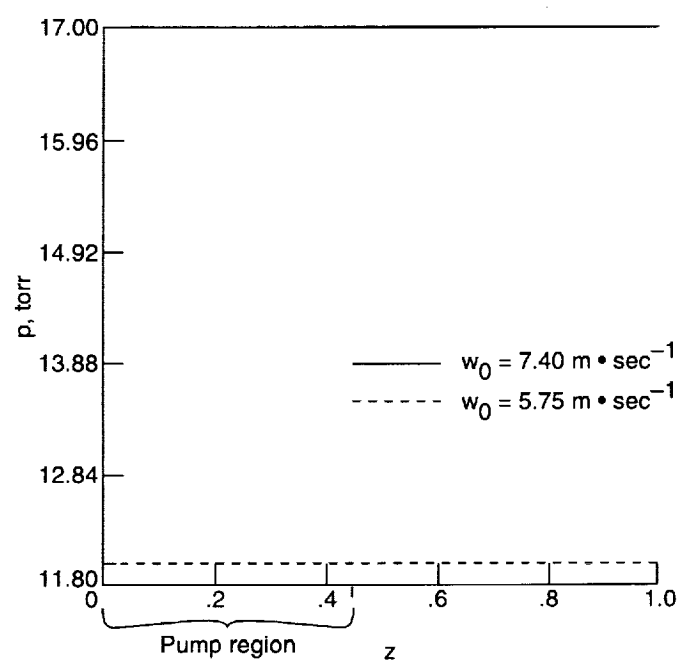
(k) Lasant pressure p versus z.

Figure 3. Concluded.
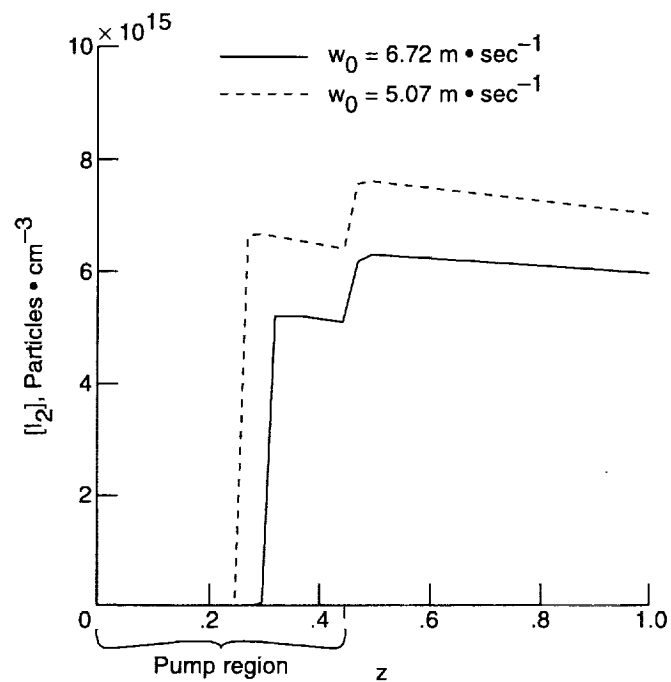
(a) Molecular iodine density $[I_2]$ versus z.
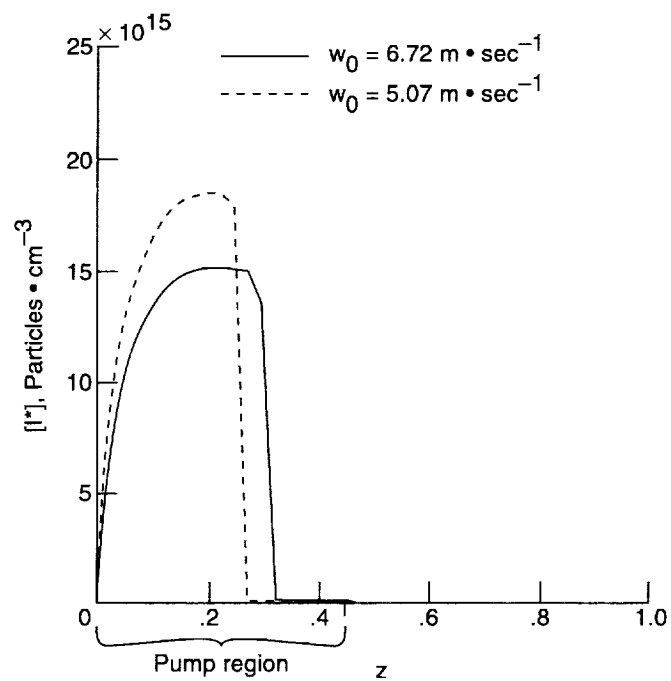
(b) Excited iodine density $[I^*]$ versus z.

Figure 4. Theoretical plots of diagnostic quantities versus z for both end points of $t1$-model curve of figure 2(a).
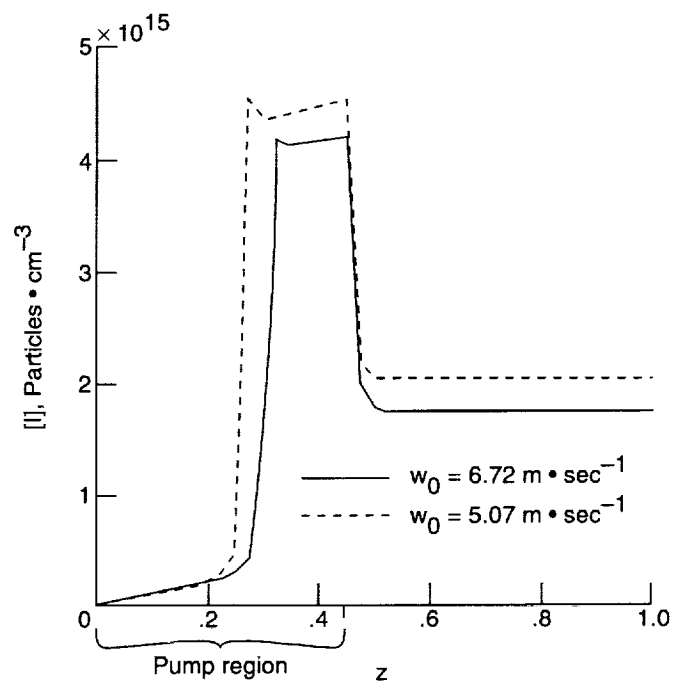
(c) Ground-state iodine density [I] versus z.
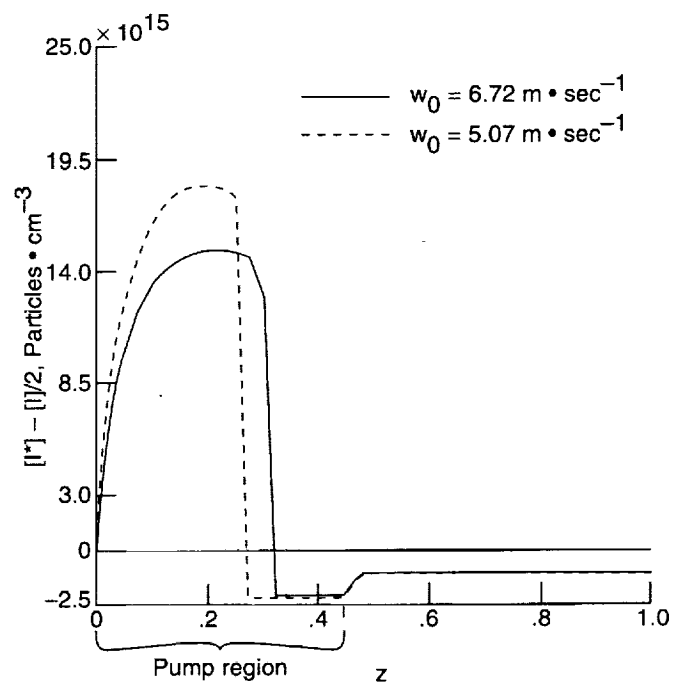
(d) Inversion density $[I^*] - [I]/2$ versus z.

Figure 4. Continued.
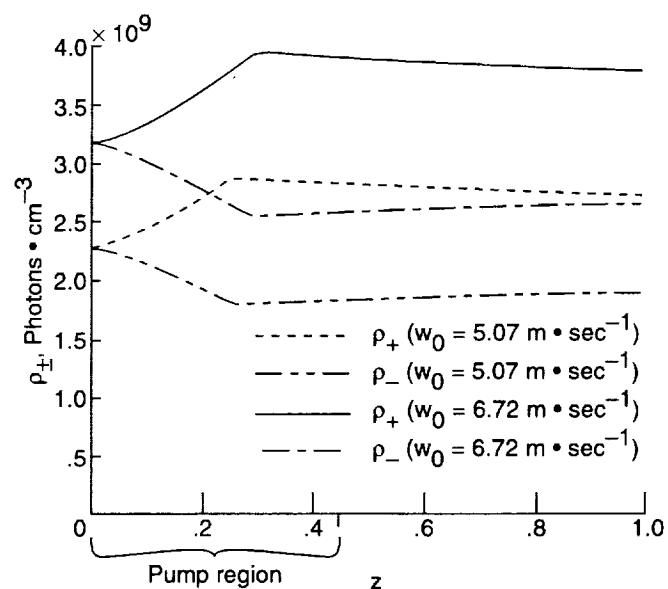
(e) Lasing photon densities ρ_+ and ρ_- versus z.
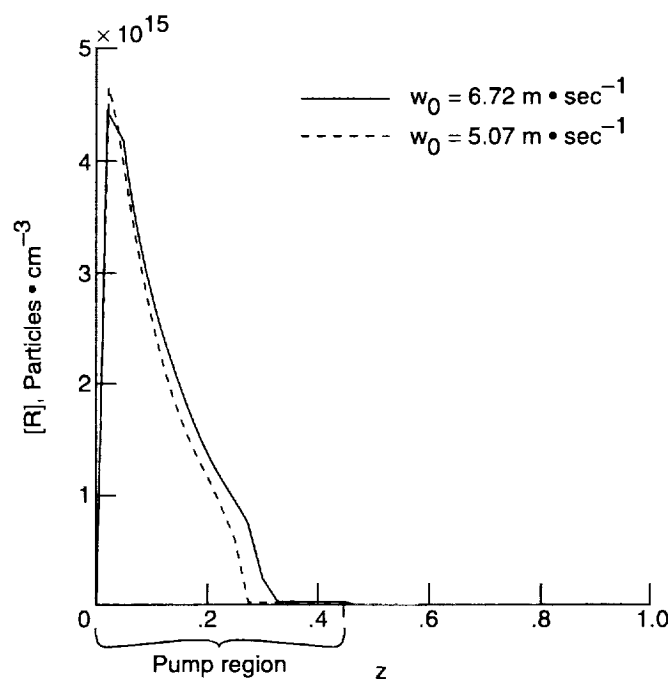
(f) Perfluoroalkyl radical density [R] versus z.

Figure 4. Continued.
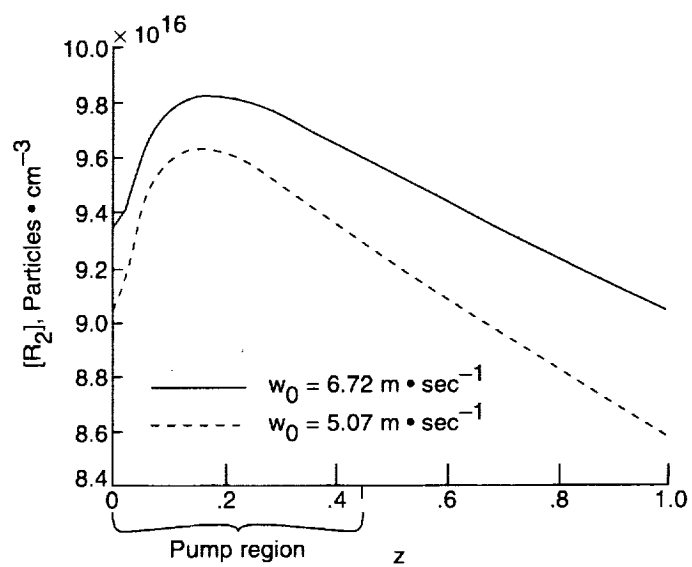
(g) Perfluoroalkyl dimer density $[R_2]$ versus z.
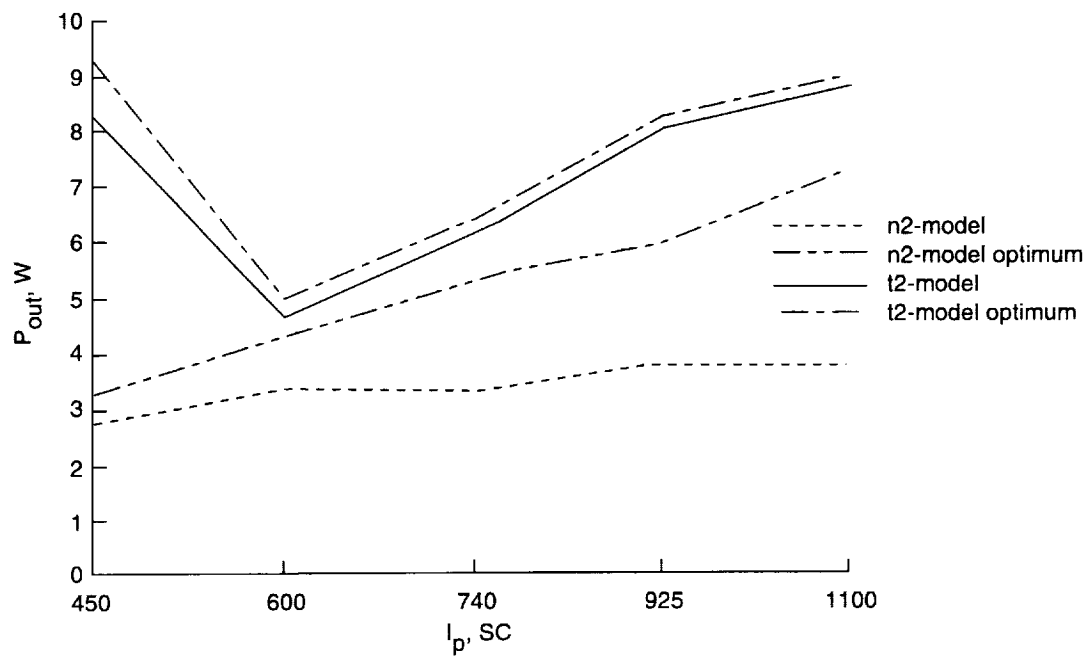
Figure 4. Concluded.

28
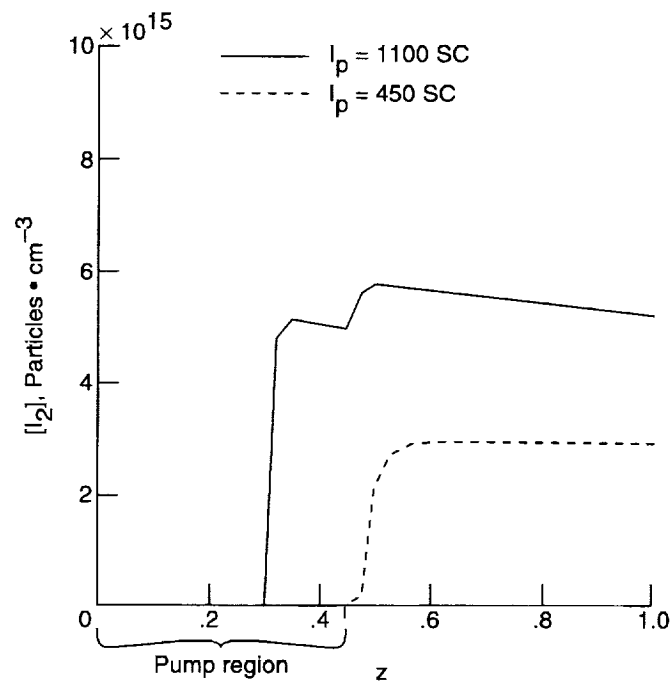
(a) Molecular iodine density $[I_2]$ versus z.
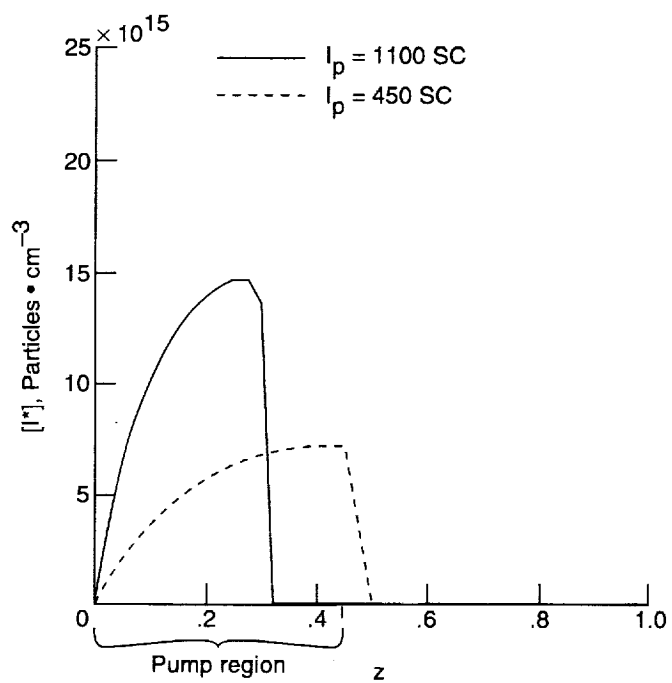
(b) Excited iodine density $[I^*]$ versus z.

Figure 5. Theoretical plots of diagnostic quantities versus z for both end points of $n2$-model curve of figure 2(b).
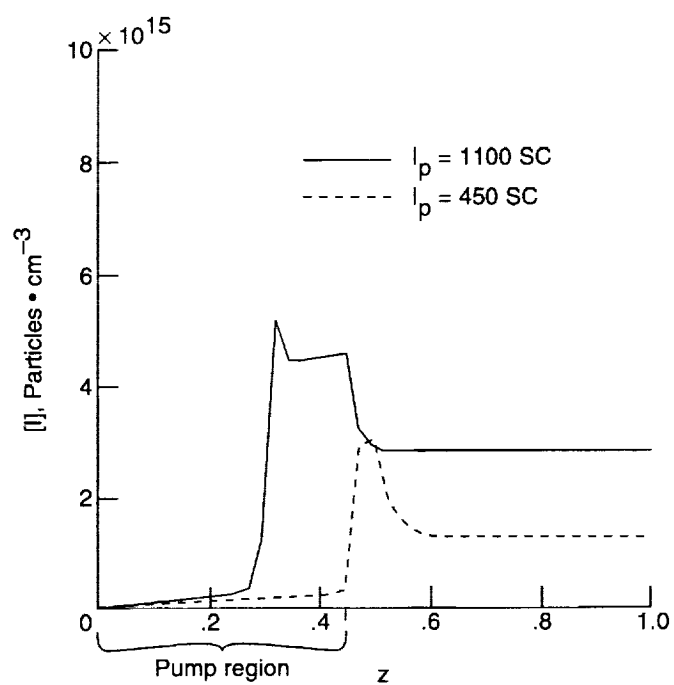
(c) Ground-state iodine density [I] versus z.
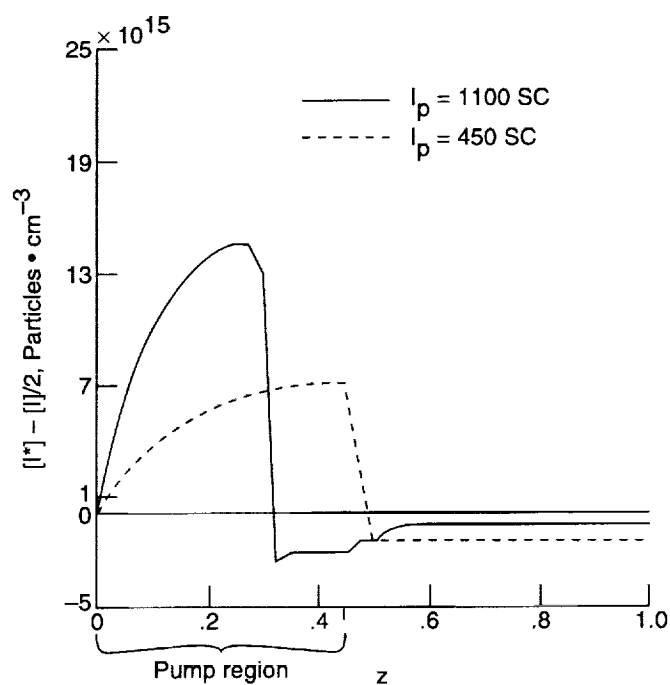
(d) Inversion density $[I^*] - [I]/2$ versus z.

Figure 5. Continued.
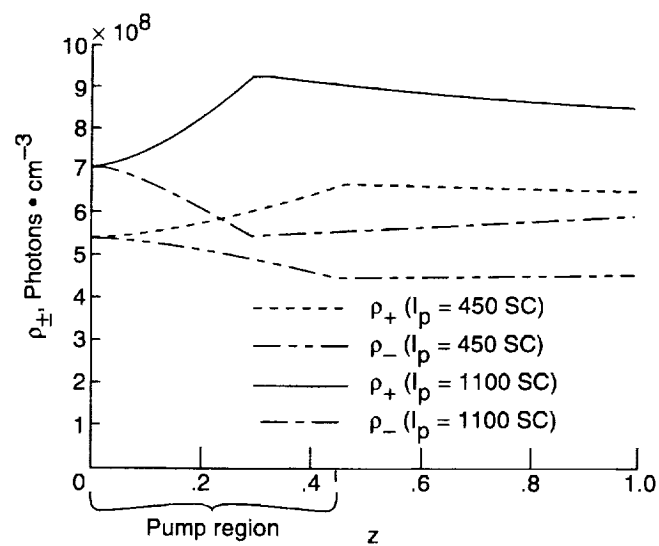
(e) Lasing photon densities ρ_+ and ρ_- versus z.
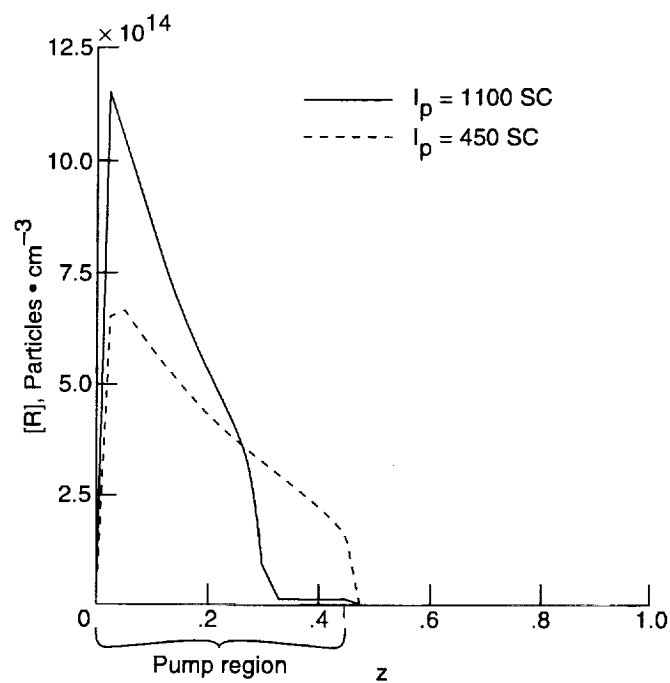
(f) Perfluoroalkyl radical density [R] versus z.

Figure 5. Continued.
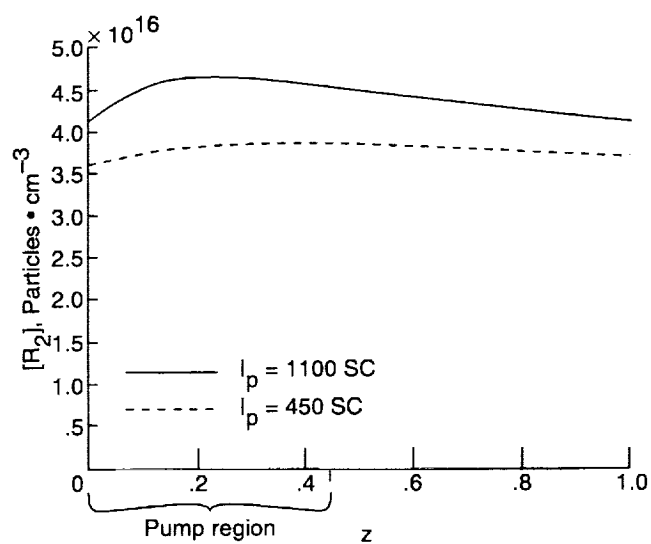
(g) Perfluoroalkyl dimer density $[R_2]$ versus z.

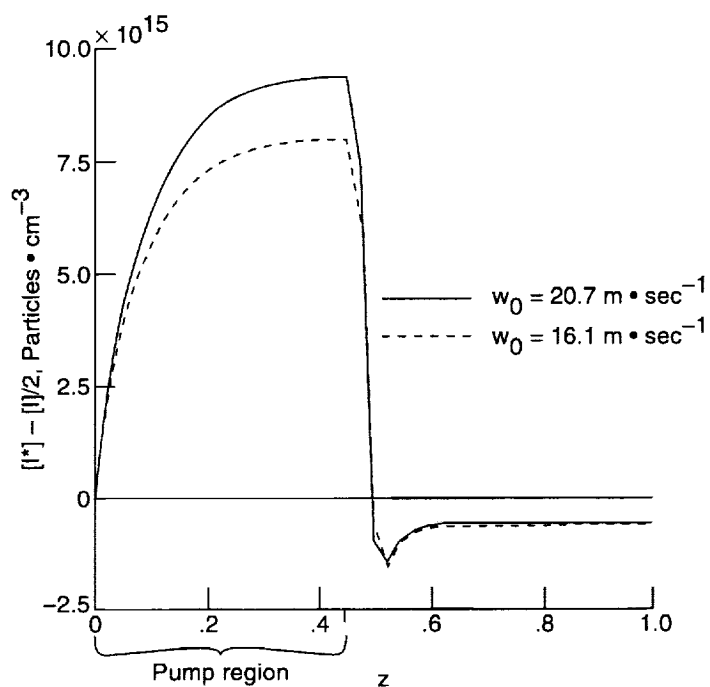Figure 5. Concluded.
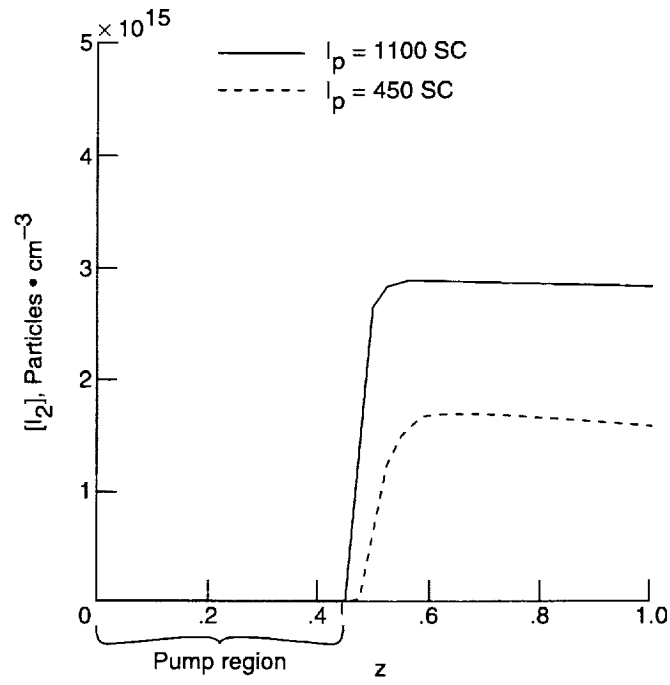
(a) Molecular iodine density $[I_2]$ versus z.
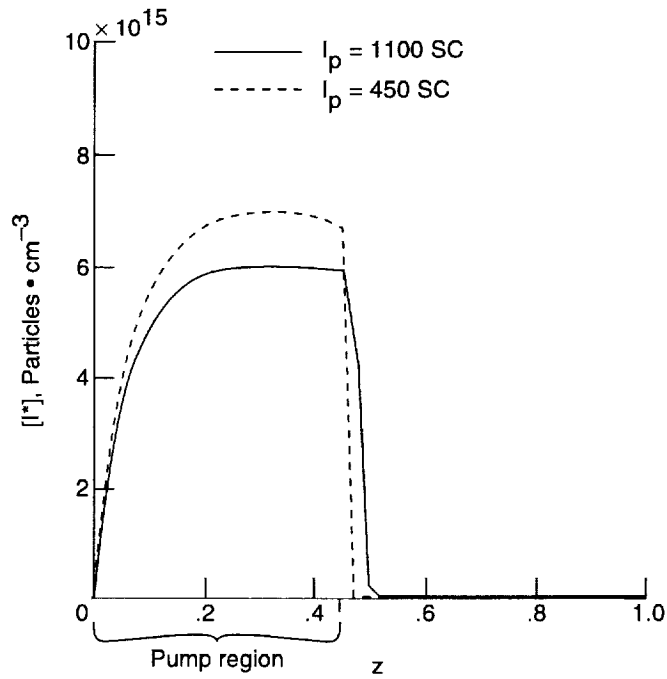
(b) Excited iodine density $[I^*]$ versus z.

Figure 6. Theoretical plots of diagnostic quantities versus z for both end points of $t2$-model curve of figure 2(b).
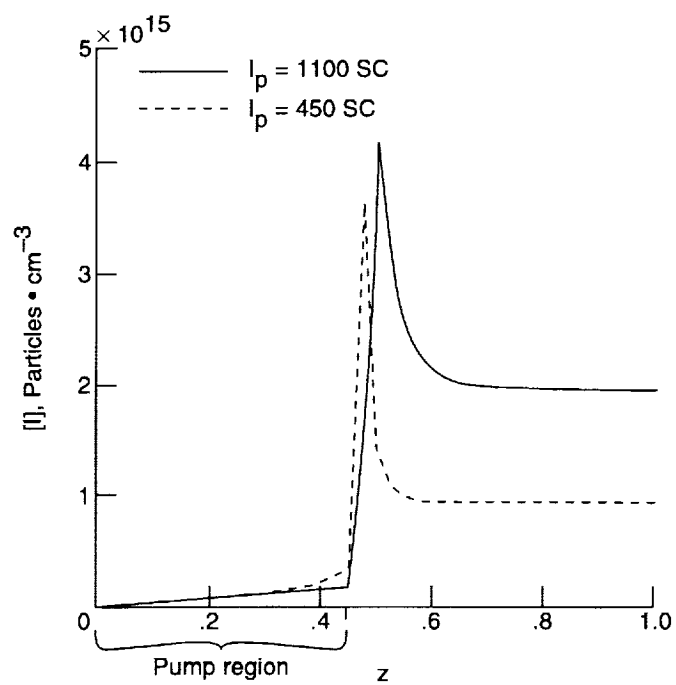
(c) Ground-state iodine density [I] versus z.
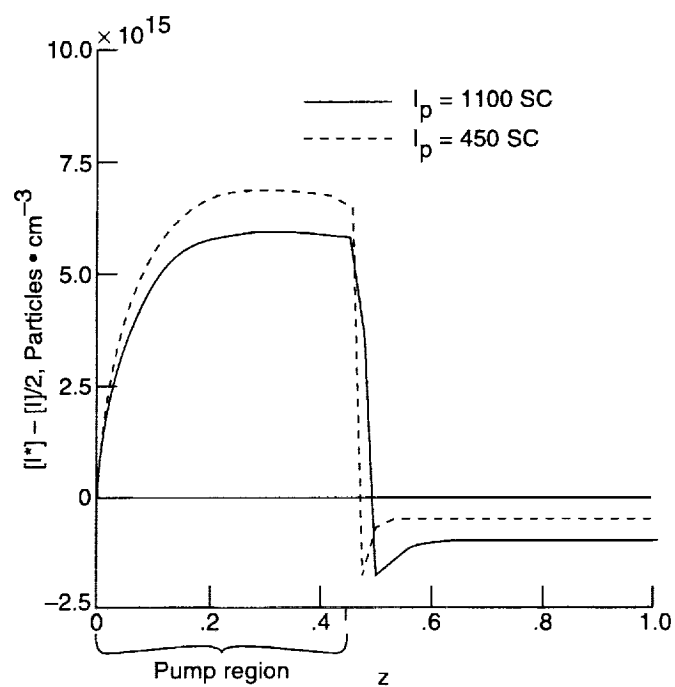
(d) Inversion density $[I^*] - [I]/2$ versus z.

Figure 6. Continued.

34
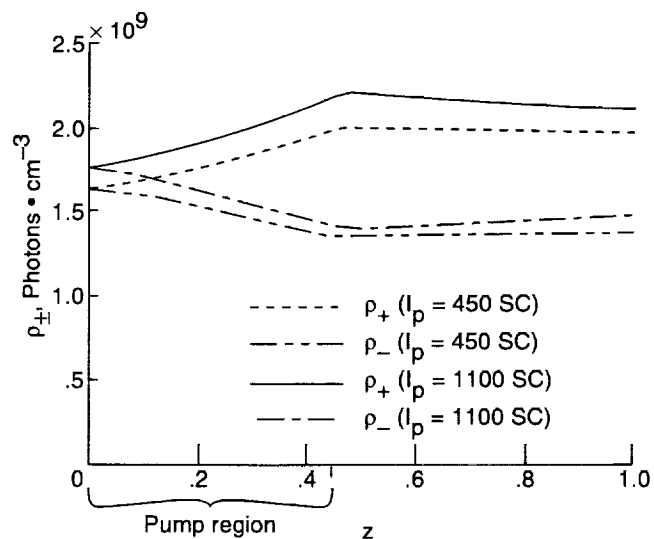
(e) Lasing photon densities ρ_+ and ρ_- versus z.
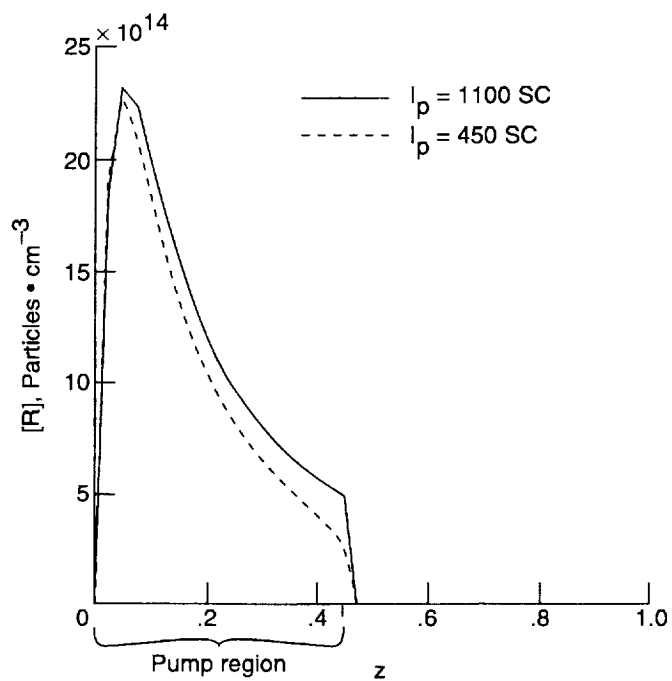
(f) Perfluoroalkyl radical density [R] versus z.

Figure 6. Continued.

35
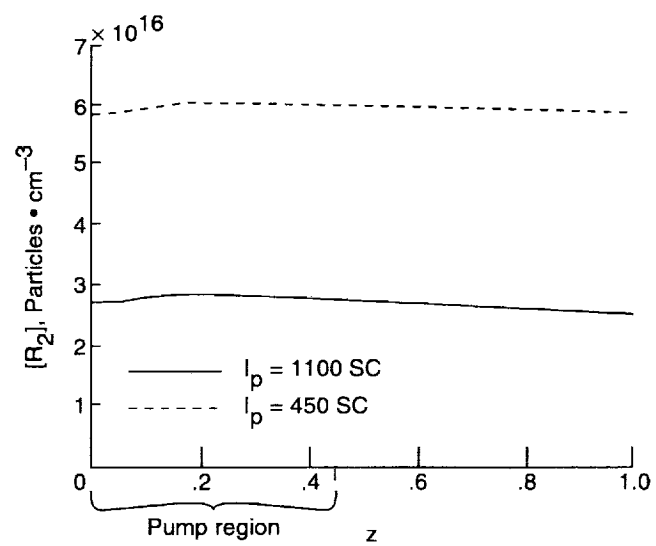
(g) Perfluoroalkyl dimer density $[R_2]$ versus z.

Figure 6. Concluded.
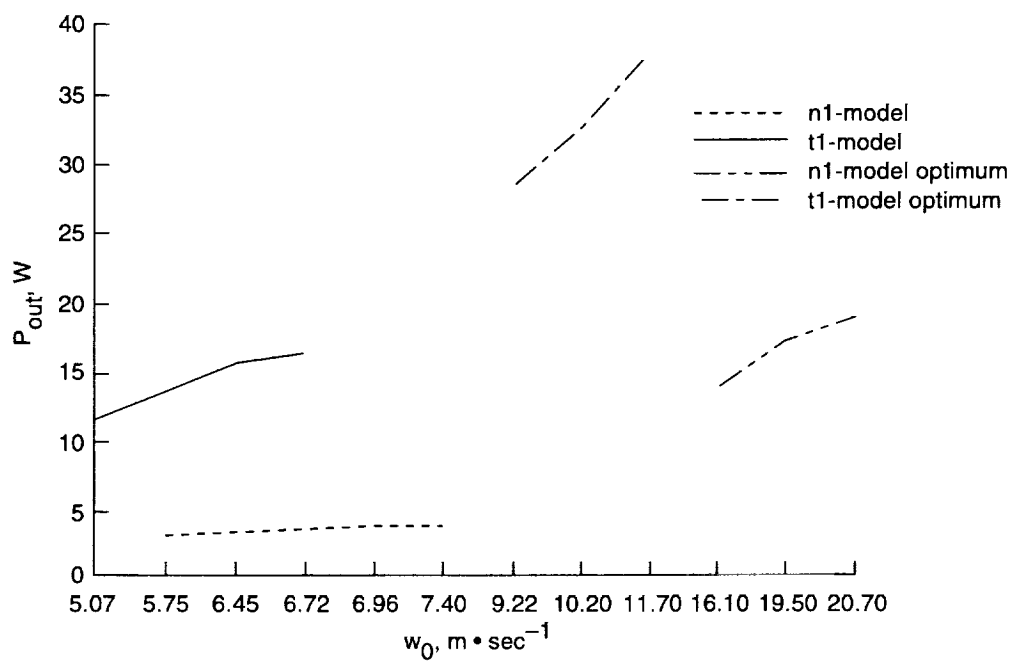
Figure 7. Theoretical effects on output power of optimized lasant flow speeds in $n1$- and $t1$-models of figure 2(a).
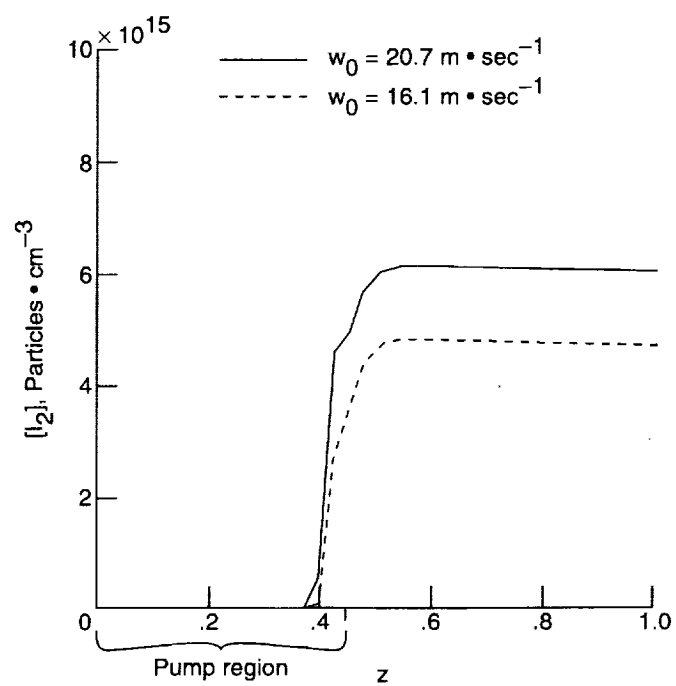
(a) Molecular iodine density $[I_2]$ versus z.
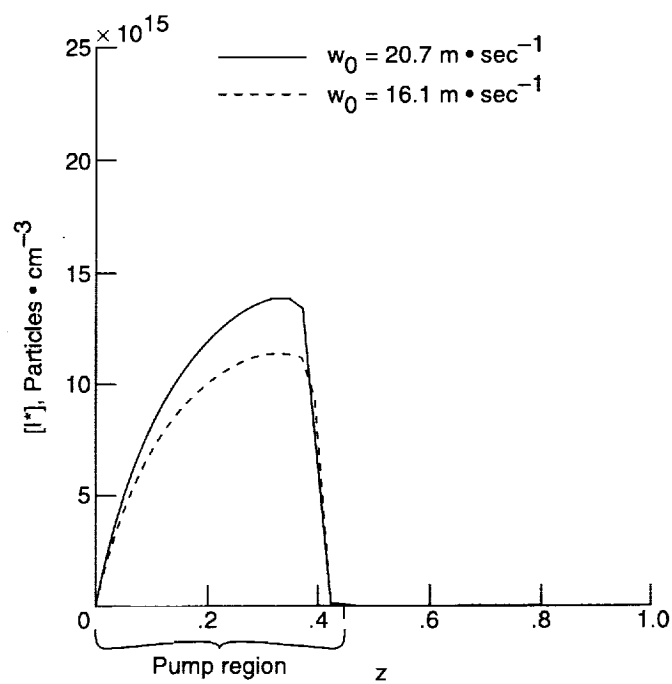
(b) Excited iodine density $[I^*]$ versus z.

Figure 8. Theoretical plots of diagnostic quantities versus z for both end points of $n1$-model optimal curve of figure 7.
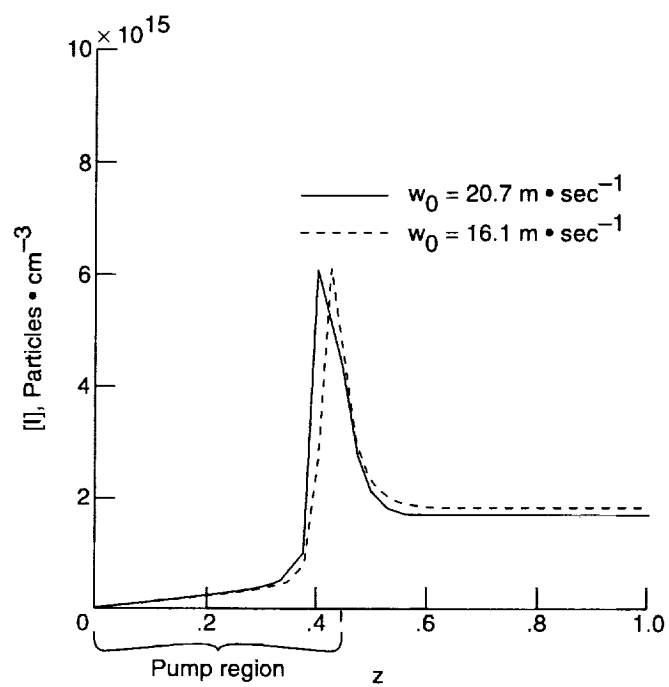
38

(c) Ground-state iodine density [I] versus z.

(d) Inversion density $[I^*] - [I]/2$ versus z.

Figure 8. Continued.

5.0×10^9

4.5

4.0

3.5

$\rho_\pm$, Photons $\cdot$ cm^{-3}

3.0

2.5

2.0

1.5

1.0

.5

———— ρ_+ $(w_0 = 20.7 \text{ m} \cdot \text{sec}^{-1})$

— $\cdot$ — ρ_- $(w_0 = 20.7 \text{ m} \cdot \text{sec}^{-1})$

- - - - ρ_+ $(w_0 = 16.1 \text{ m} \cdot \text{sec}^{-1})$

— $\cdot\cdot$ — ρ_- $(w_0 = 16.1 \text{ m} \cdot \text{sec}^{-1})$

0   .2   .4   .6   .8   1.0

Pump region z

(e) Lasing photon densities ρ_+ and ρ_- versus z.

25×10^{14}

20

[R], Particles $\cdot$ cm^{-3}

15

10

5

———— $w_0 = 20.7 \text{ m} \cdot \text{sec}^{-1}$

- - - - $w_0 = 16.1 \text{ m} \cdot \text{sec}^{-1}$

0   .2   .4   .6   .8   1.0

Pump region z
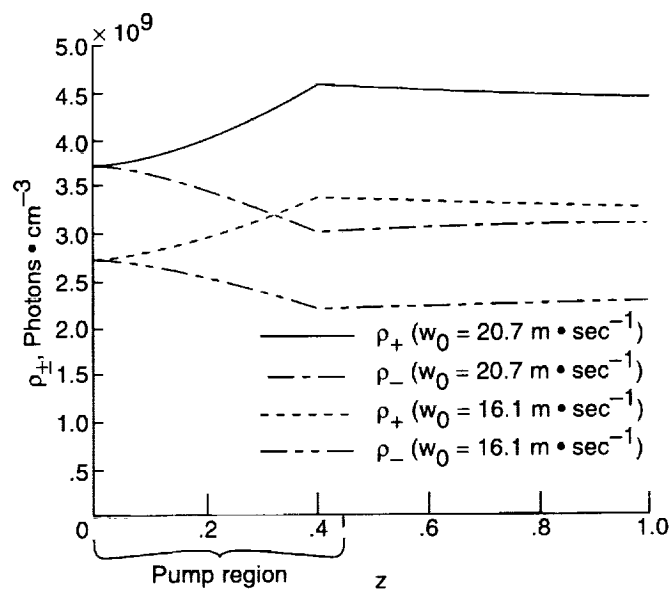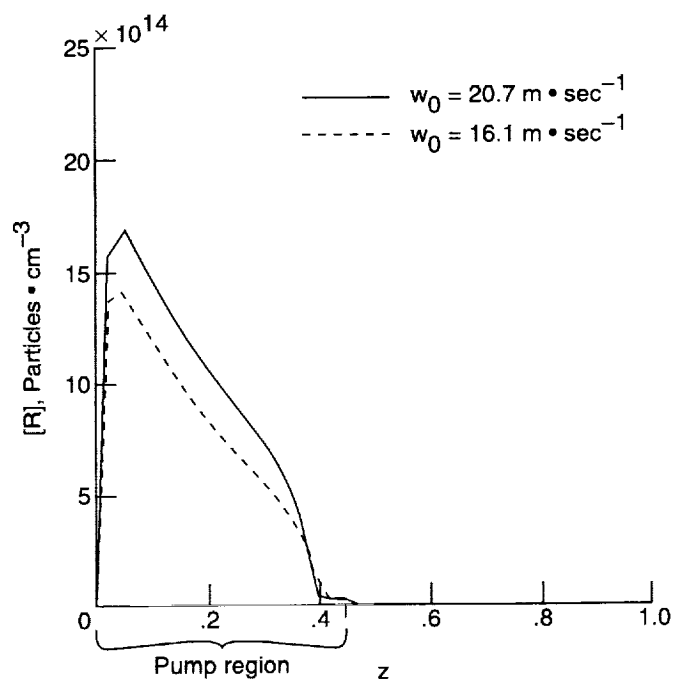
(f) Perfluoroalkyl radical density [R] versus z.

Figure 8. Continued.

40
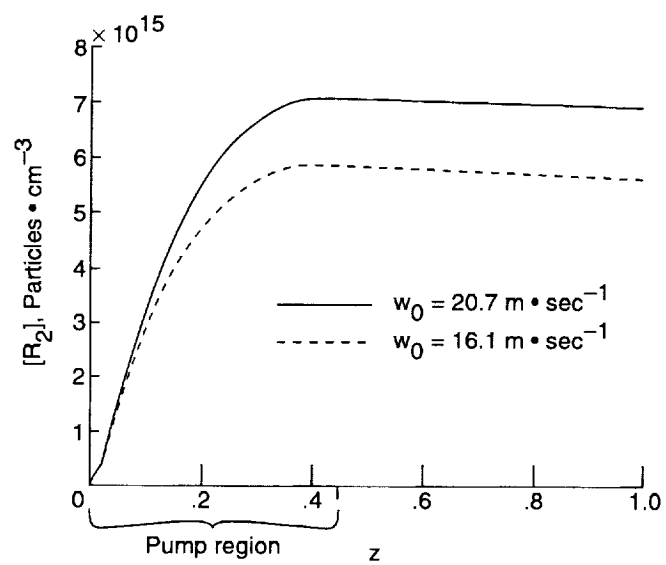
(g) Perfluoroalkyl dimer density $[R_2]$ versus z.

Figure 8. Concluded.
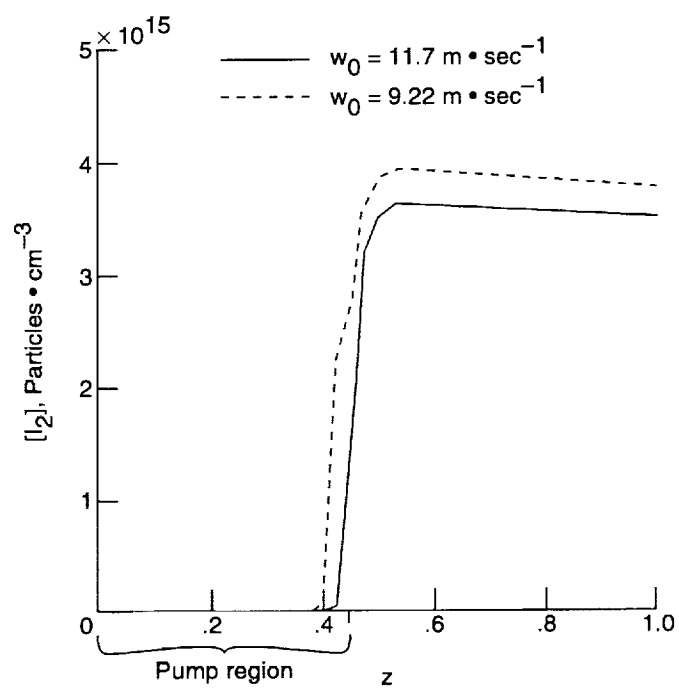
(a) Molecular iodine density $[I_2]$ versus z.
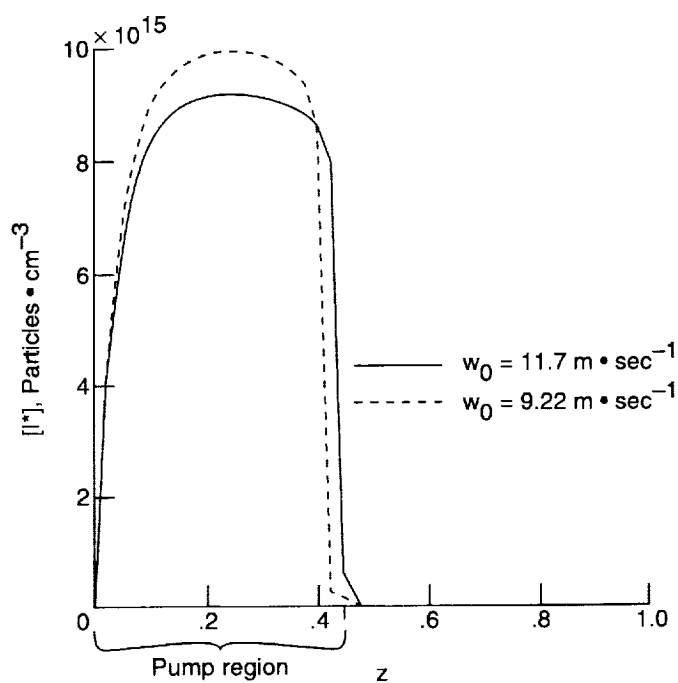
(b) Excited iodine density $[I^*]$ versus z.

Figure 9. Theoretical plots of diagnostic quantities versus z for both end points of $t1$-model optimal curve of figure 7.
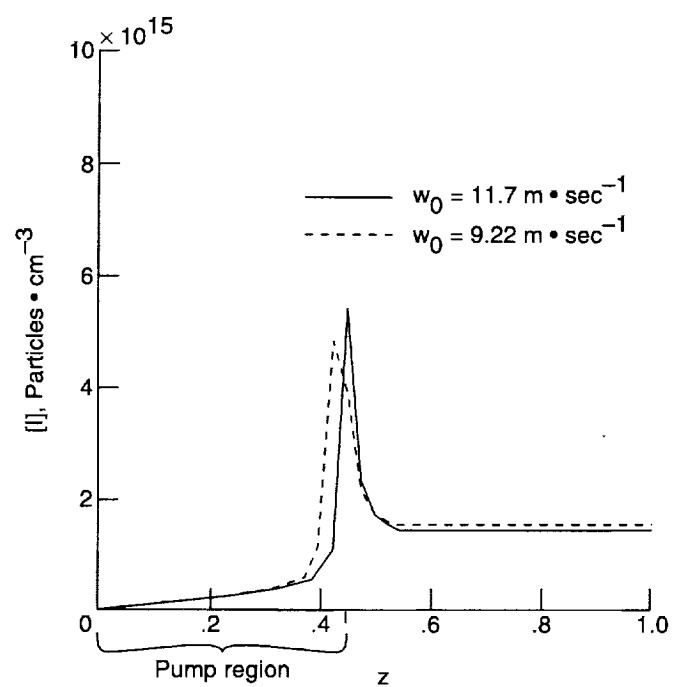
(c) Ground-state iodine density [I] versus z.
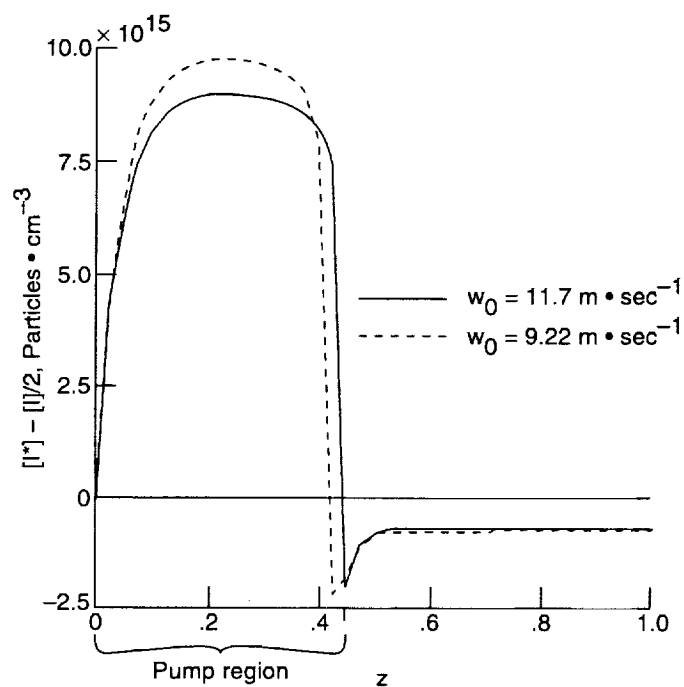
(d) Inversion density $[I^*] - [I]/2$ versus z.

Figure 9. Continued.
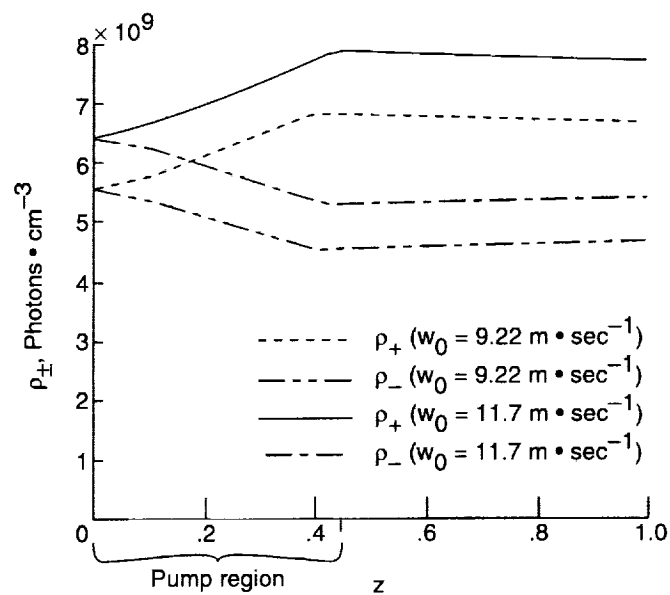
(e) Lasing photon densities ρ_+ and ρ_- versus z.
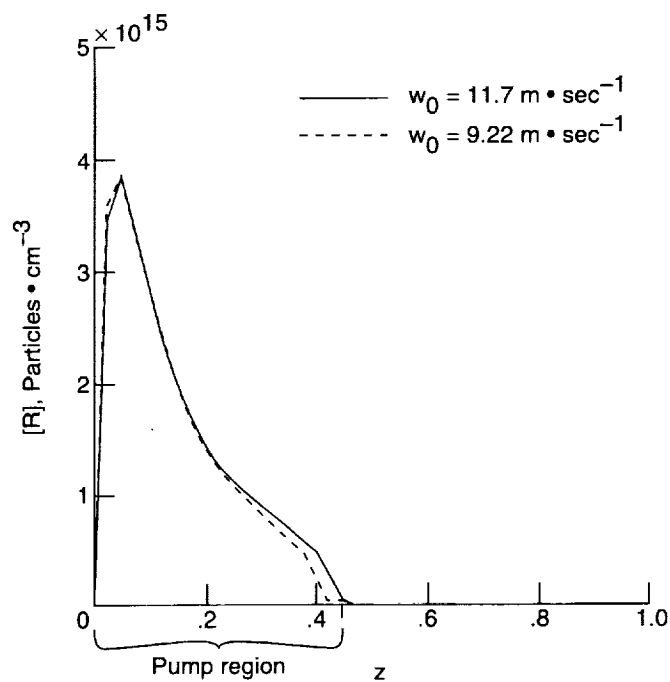
(f) Perfluoroalkyl radical density [R] versus z.

Figure 9. Continued.
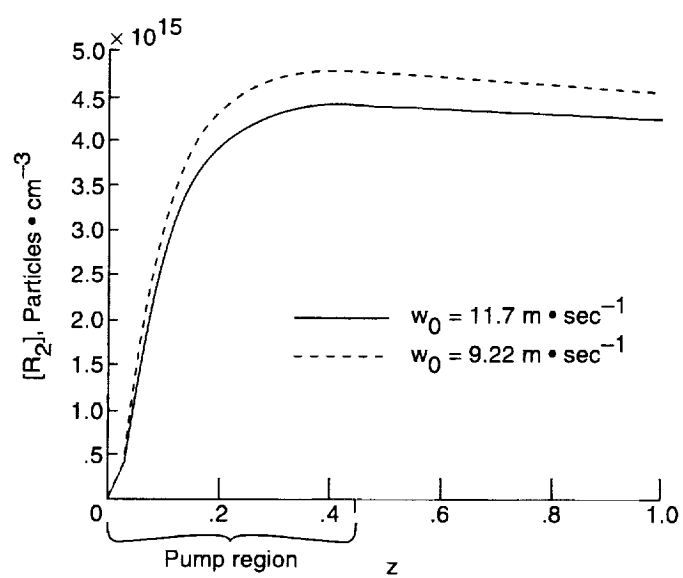
(g) Perfluoroalkyl dimer density $[R_2]$ versus z.

Figure 9. Concluded.

Figure 10. Theoretical effects on output power of optimized lasant flow speeds in $n2$- and $t2$-models of figure 2(b).
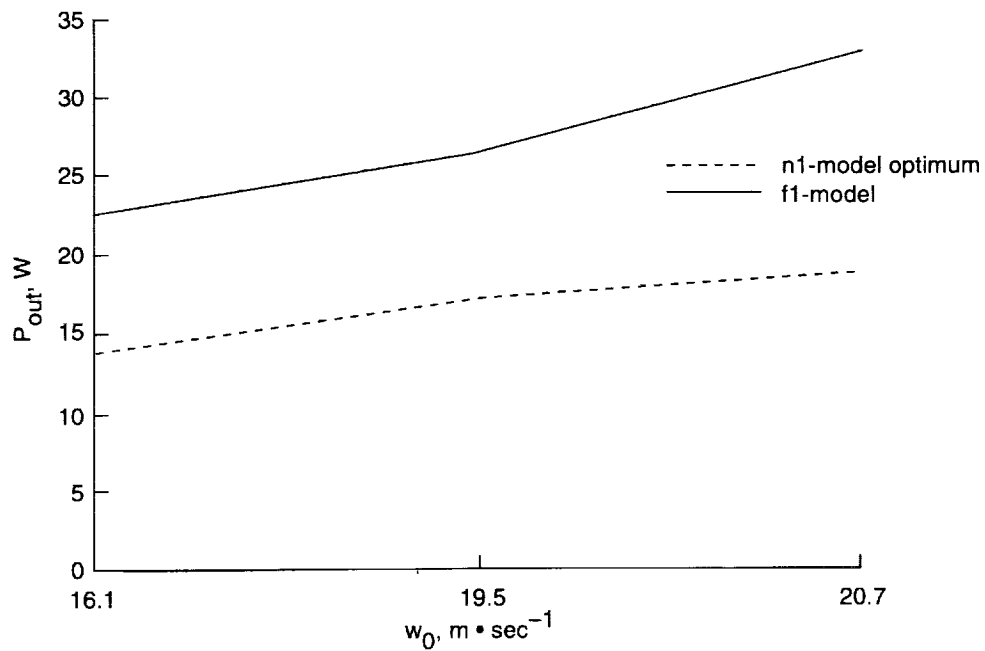
Figure 11. Theoretical comparison of output power from fictional $f1$-model and $n1$-model optimum of figure 7.
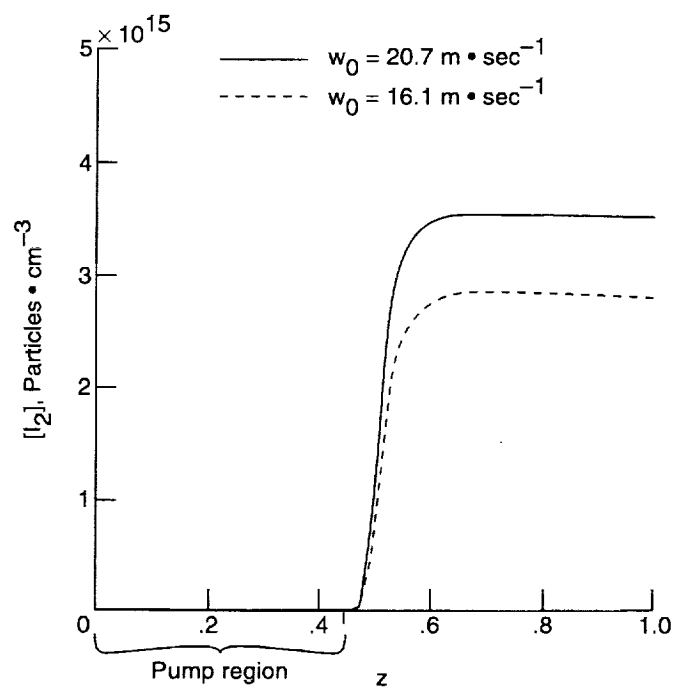
(a) Molecular iodine density $[I_2]$ versus z.
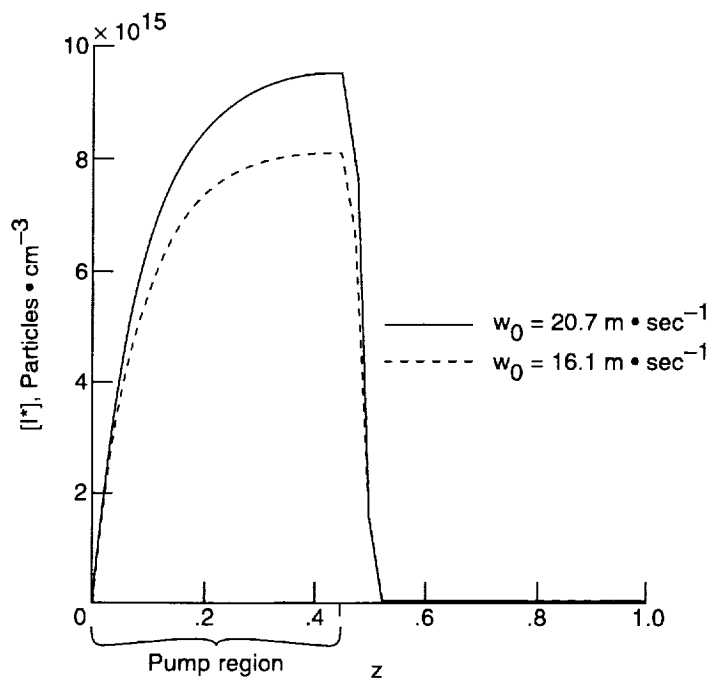
(b) Excited iodine density $[I^*]$ versus z.

Figure 12. Theoretical plots of diagnostic quantities versus z for both end points of fictional $f1$-model curve of figure 11.
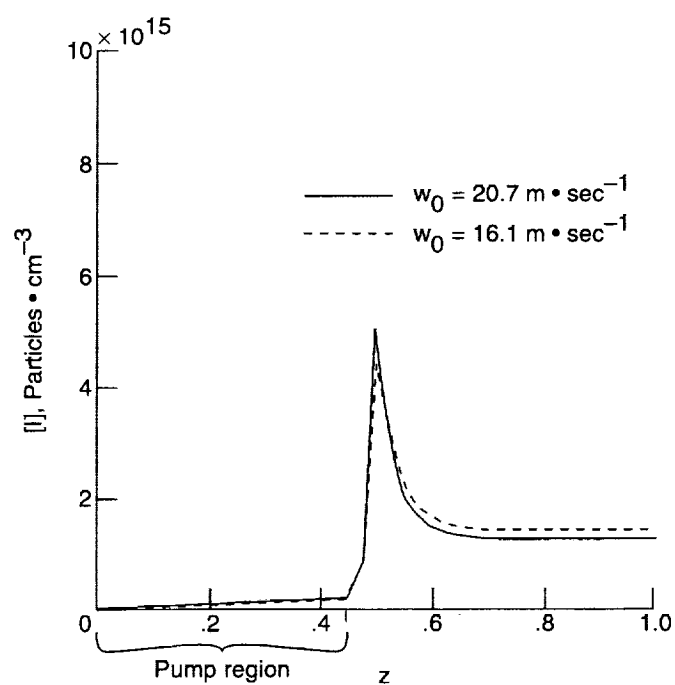
(c) Ground-state iodine density [I] versus z.

(d) Inversion density $[I^*] - [I]/2$ versus z.

Figure 12. Continued.

48
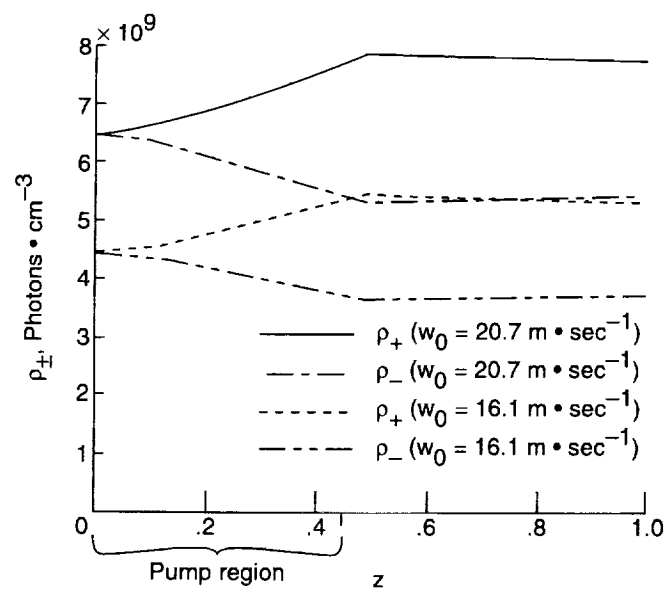
(e) Lasing photon densities ρ_+ and ρ_- versus z.
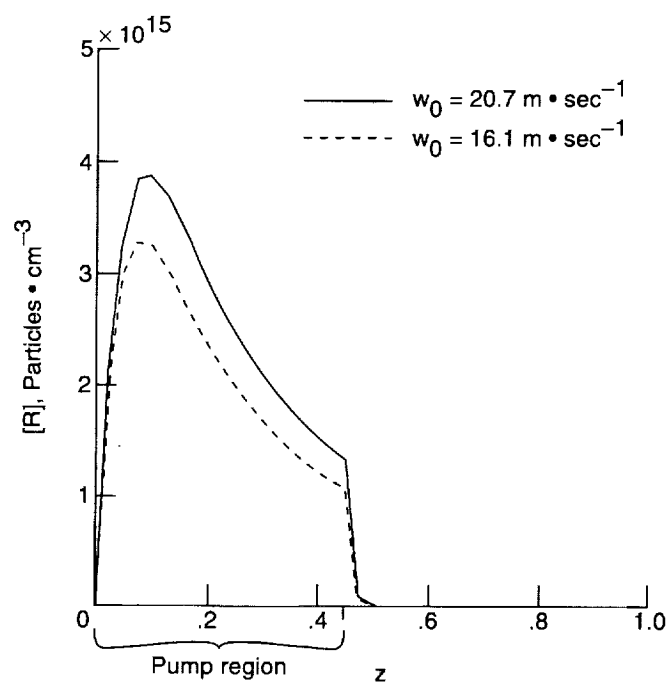
(f) Perfluoroalkyl radical density [R] versus z.

Figure 12. Continued.
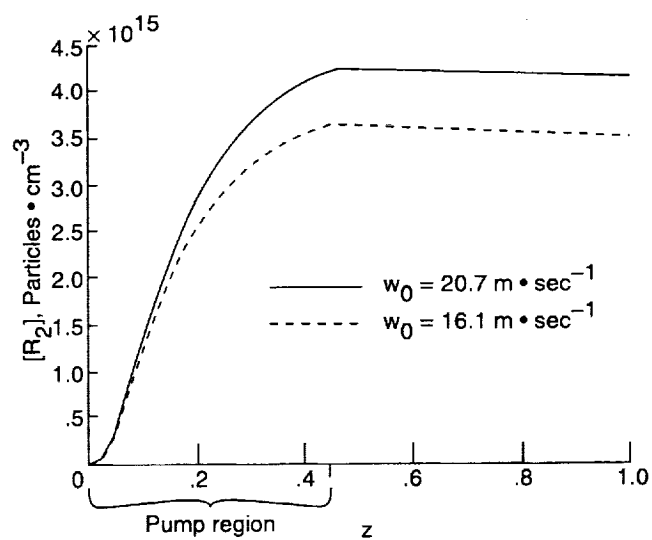
(g) Perfluoroalkyl dimer density $[R_2]$ versus z.

Figure 12. Concluded.
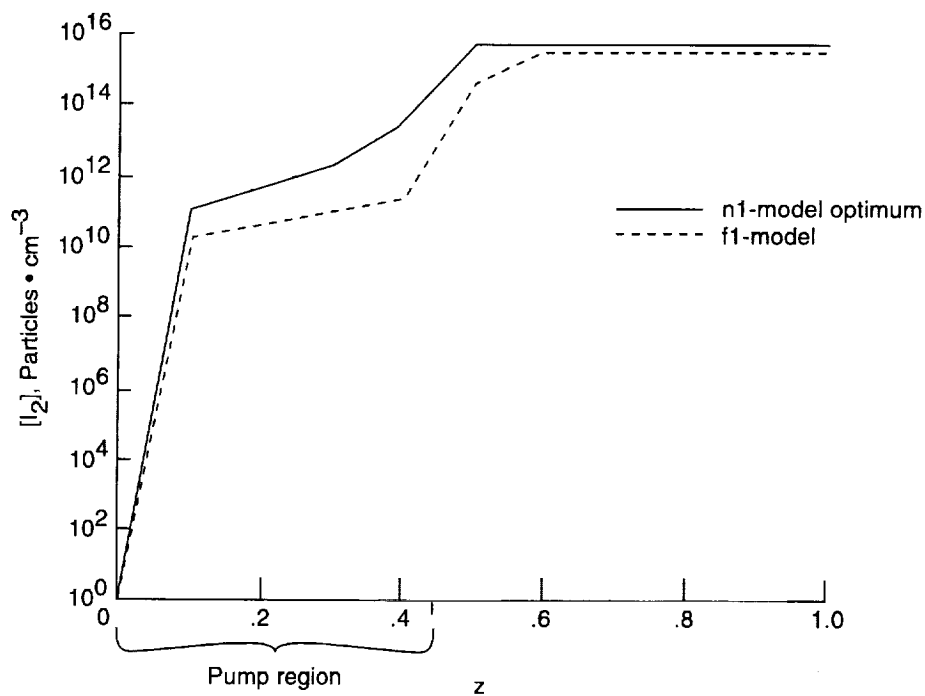
(a) Molecular iodine density $[I_2]$ versus z.
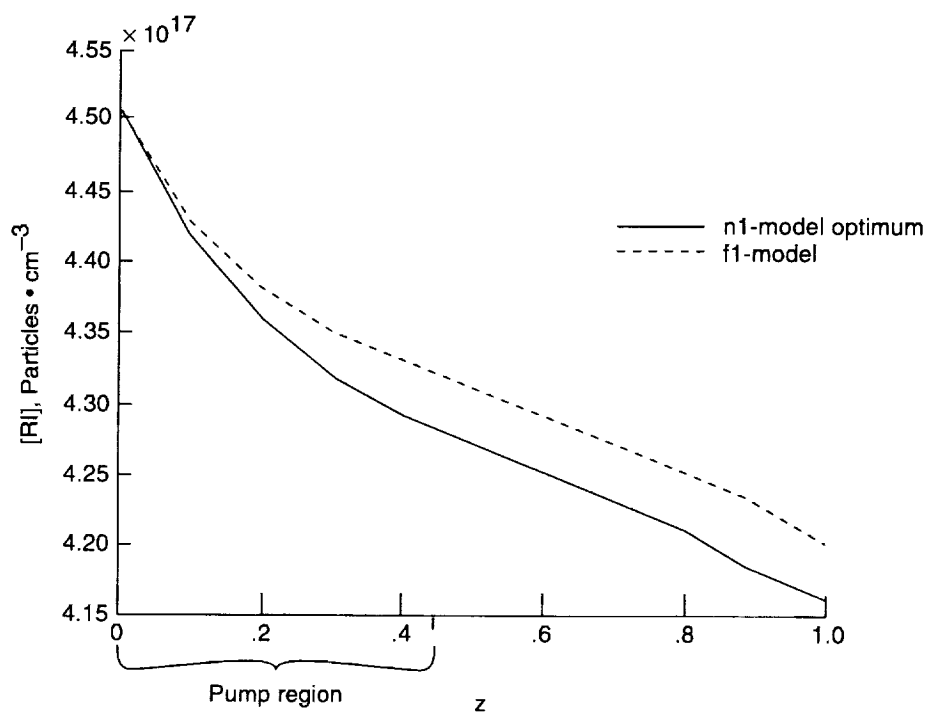
(b) Lasant number density [RI] versus z.

Figure 13. Detailed theoretical plots of fictitious $f1$-model and $n1$-model optimum of figure 11 at $w_0 = 19.5$ m · sec^{-1}.
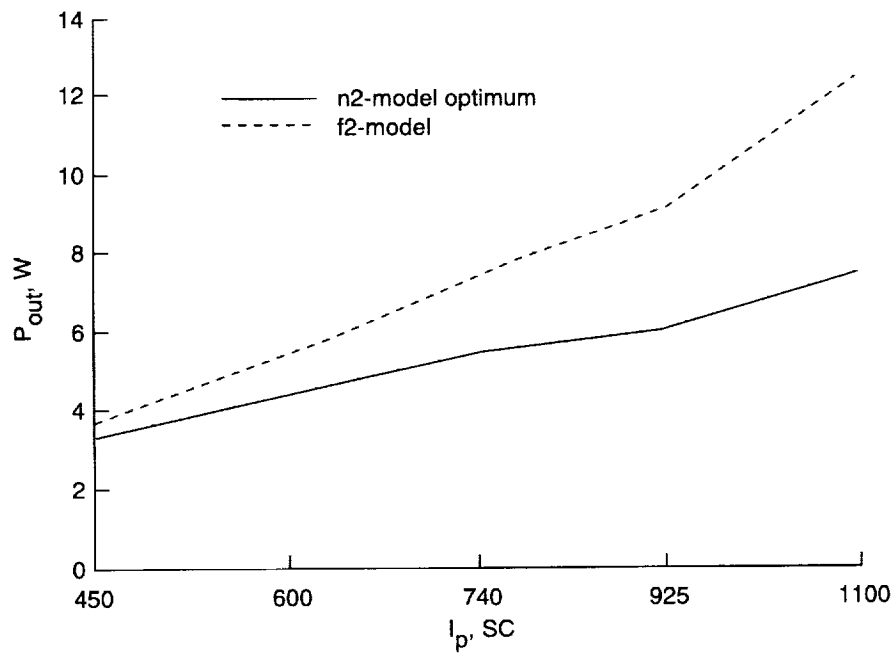
Figure 14. Theoretical comparison of output power from fictitious $f2$-model and $n2$-model optimum of figure 10.
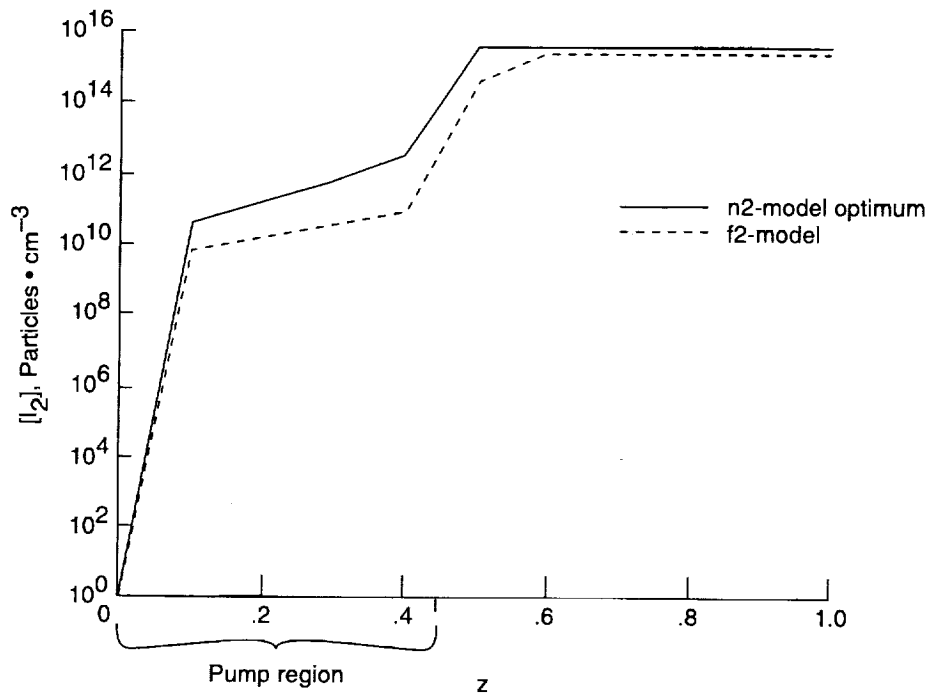
(a) Molecular iodine density $[I_2]$ versus z.
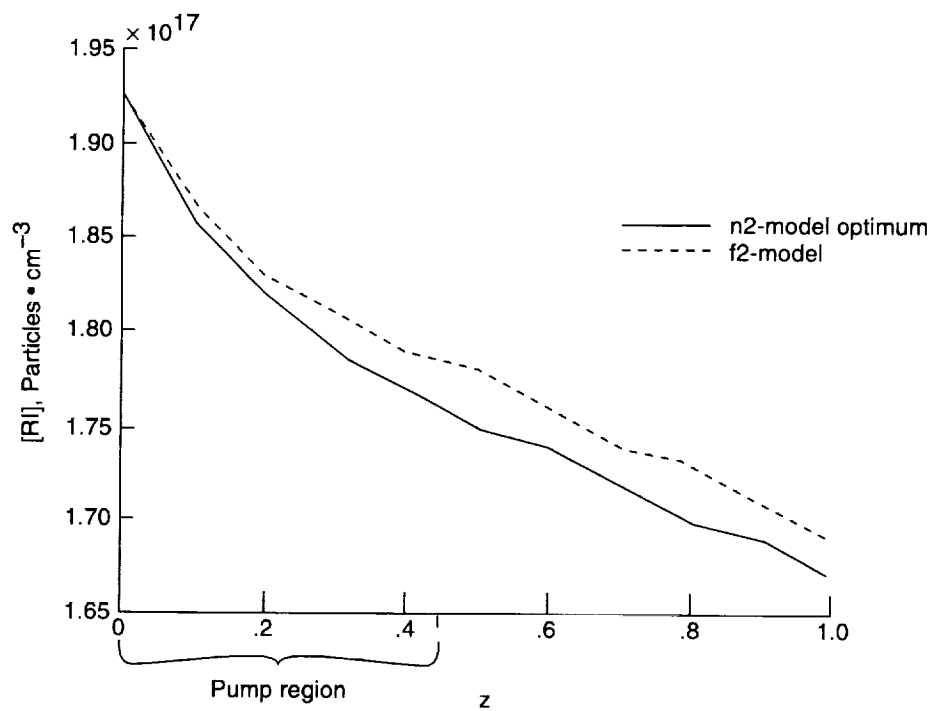
(b) Lasant number density [RI] versus z.

Figure 15. Detailed theoretical plots for fictitious $f2$-model and $n2$-model optimum of figure 14 at $I_p = 740$ SC.
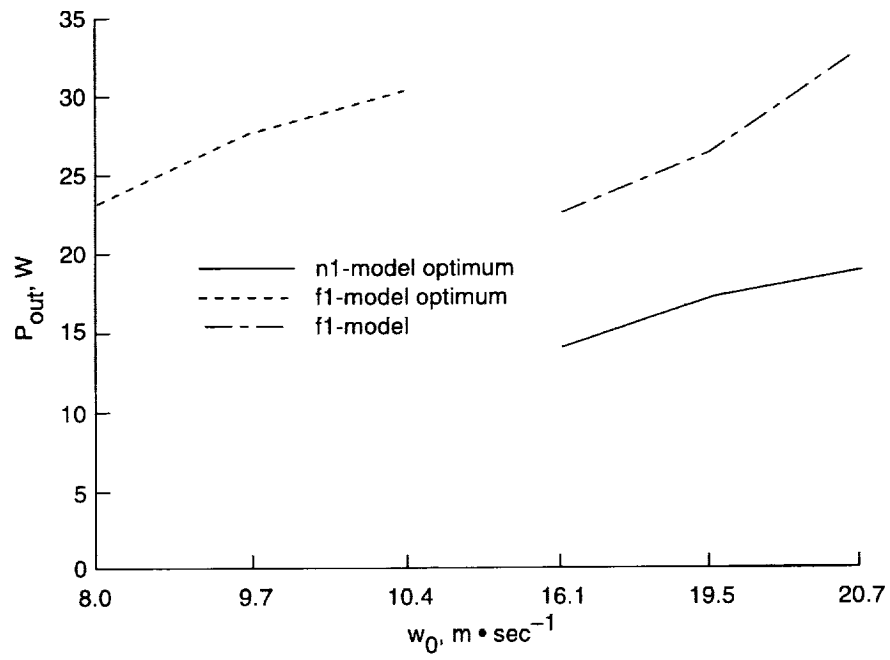
Figure 16. Theoretical comparison of output power from $n1$-model optimum and fictitious $f1$-model of figure 11 with $f1$-model optimized by halving the lasant flow speeds.
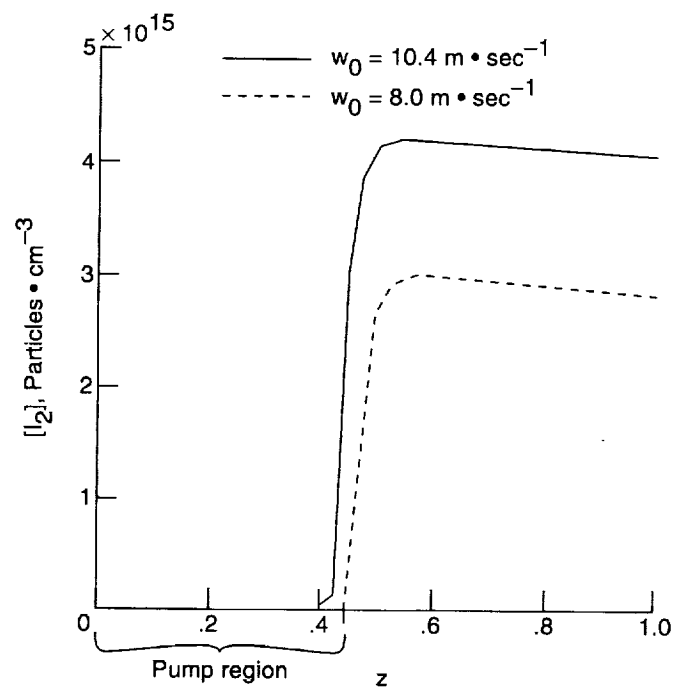
(a) Molecular iodine density $[I_2]$ versus z.
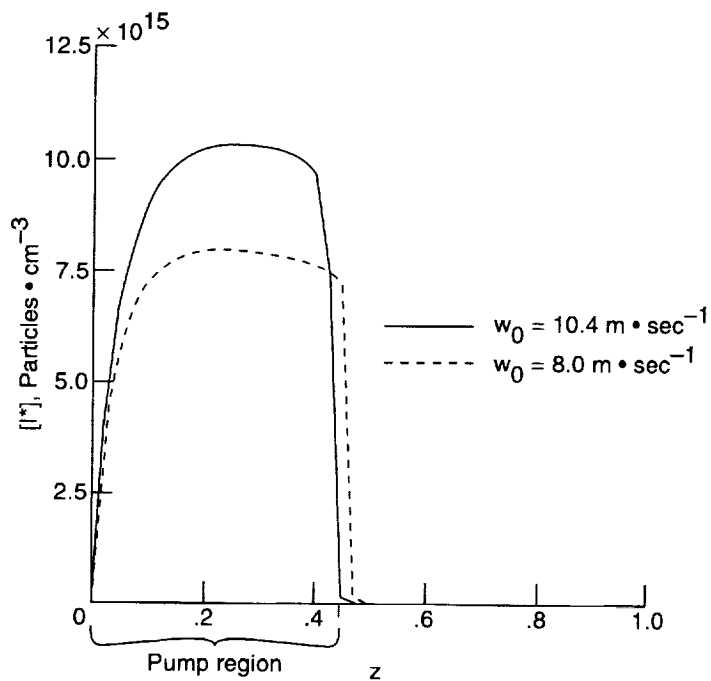
(b) Excited iodine density $[I^*]$ versus z.

Figure 17. Theoretical plots of diagnostic quantities versus z for both end points of fictitious $f1$-model optimal curve of figure 16.
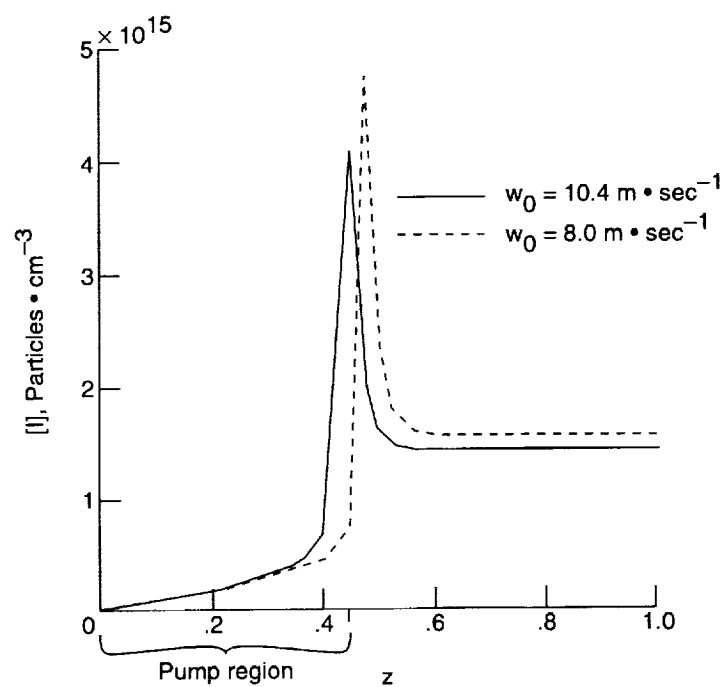
(c) Ground-state iodine density [I] versus z.
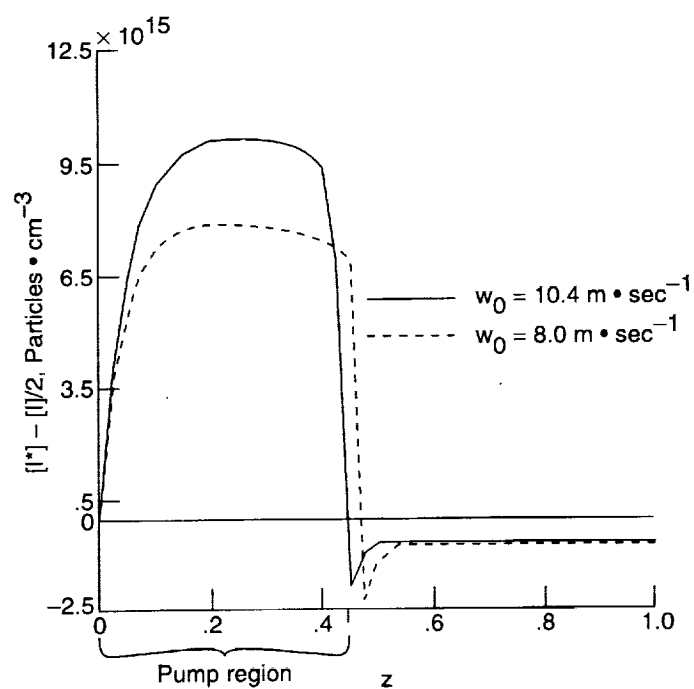
(d) Inversion density $[I^*] - [I]/2$ versus z.

Figure 17. Continued.
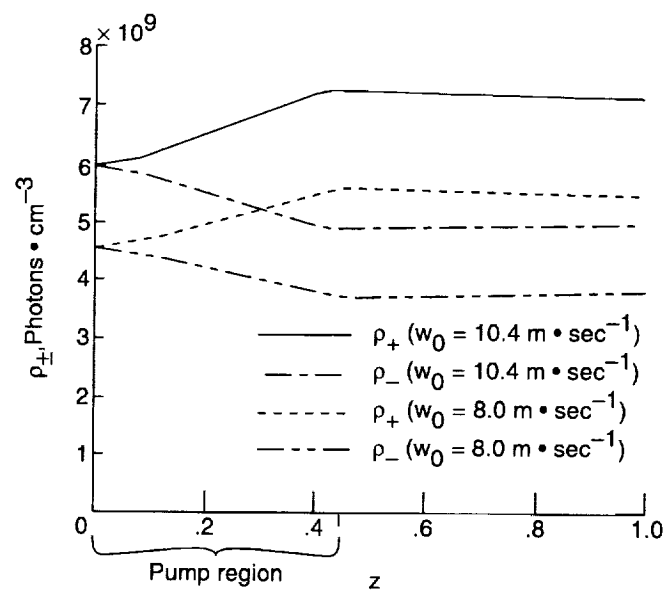
(e) Lasing photon densities ρ_+ and ρ_- versus z.
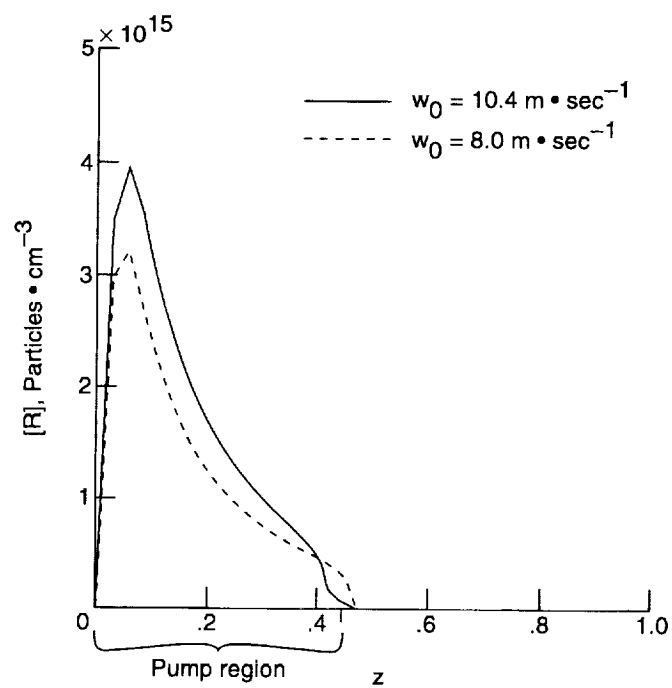
(f) Perfluoroalkyl radical density [R] versus z.

Figure 17. Continued.
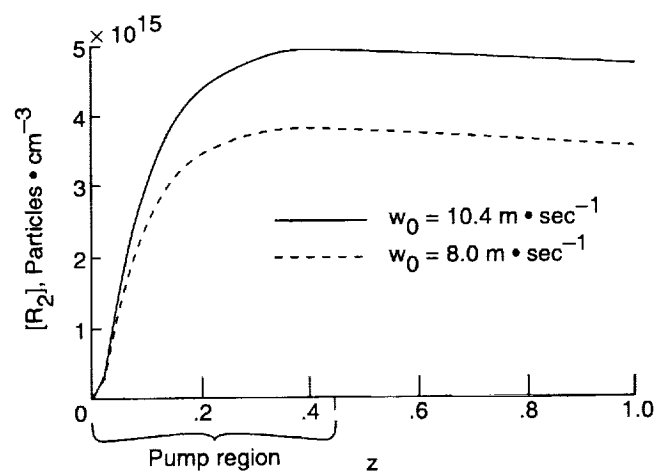
(g) Perfluoroalkyl dimer density $[R_2]$ versus z.

Figure 17. Concluded.
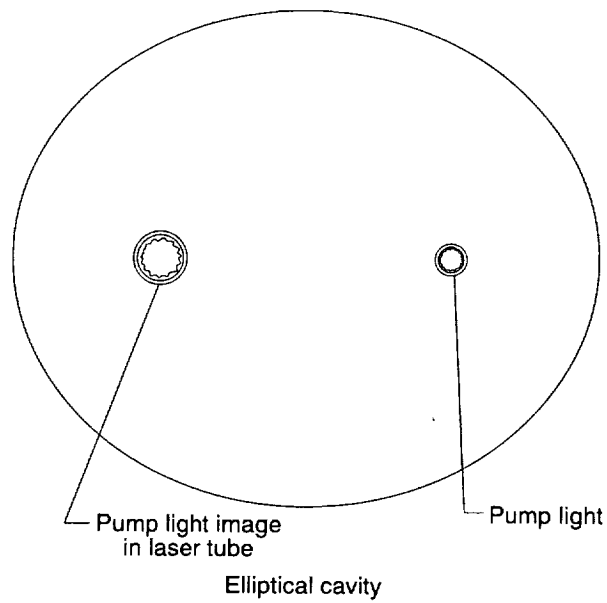
Figure 18. Cross section of elliptical pump chamber.
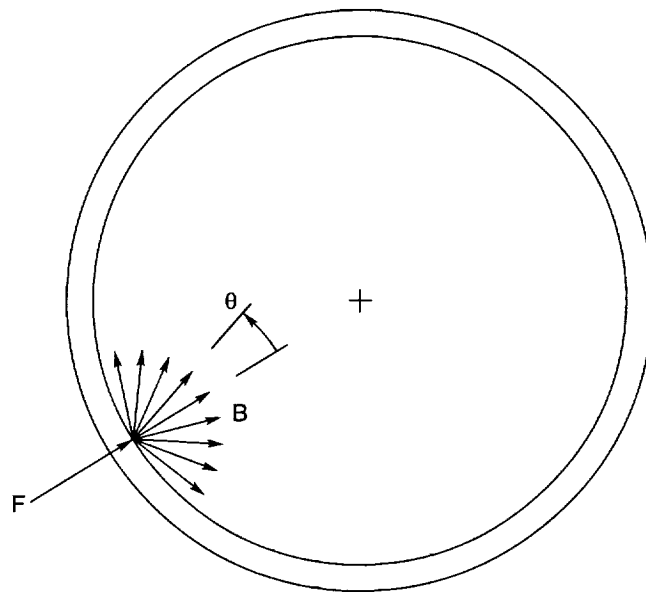
Figure 19. Cross section of laser tube with pump image brightness B and incident flux F.
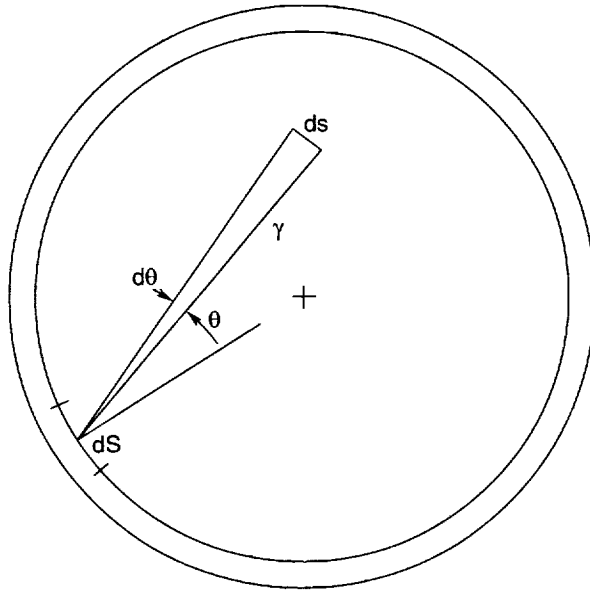
Figure 20. Cross section of laser tube with ray geometry.
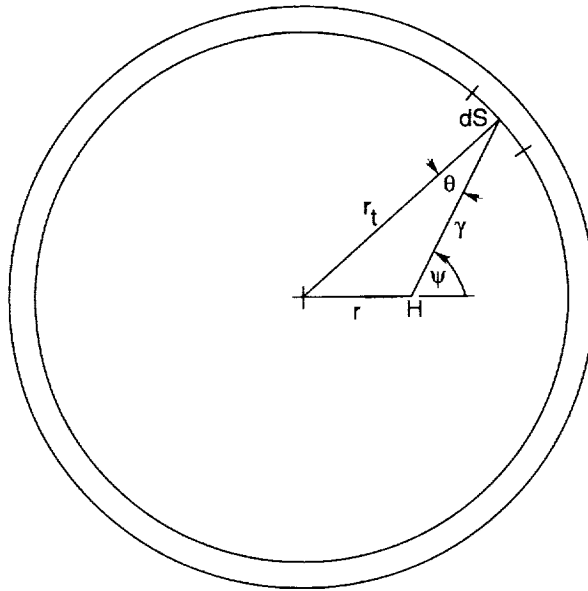
Figure 21. Cross section of laser tube with geometry for computing total pumping photon energy density at radius r in absorbing lasant.
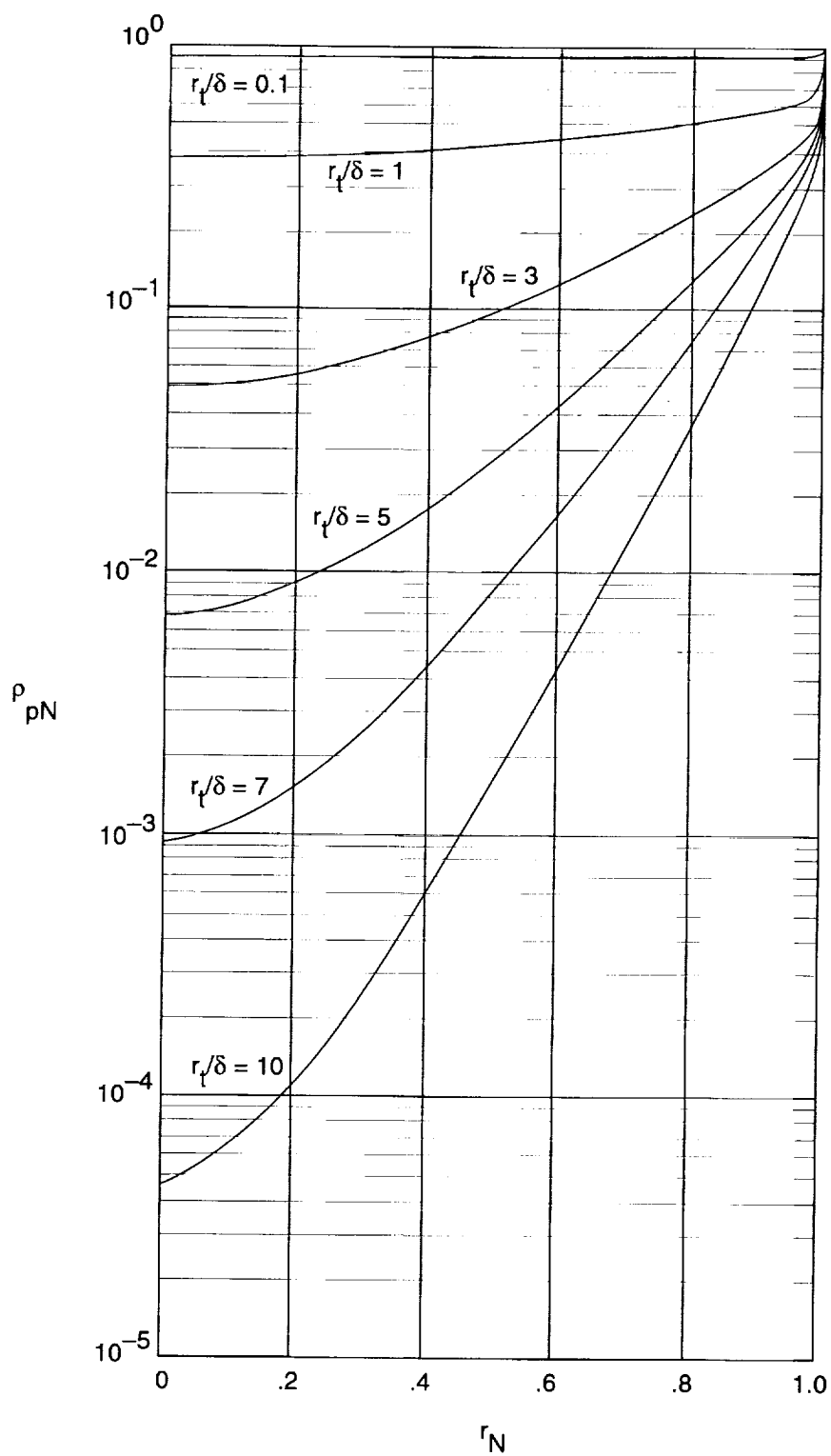
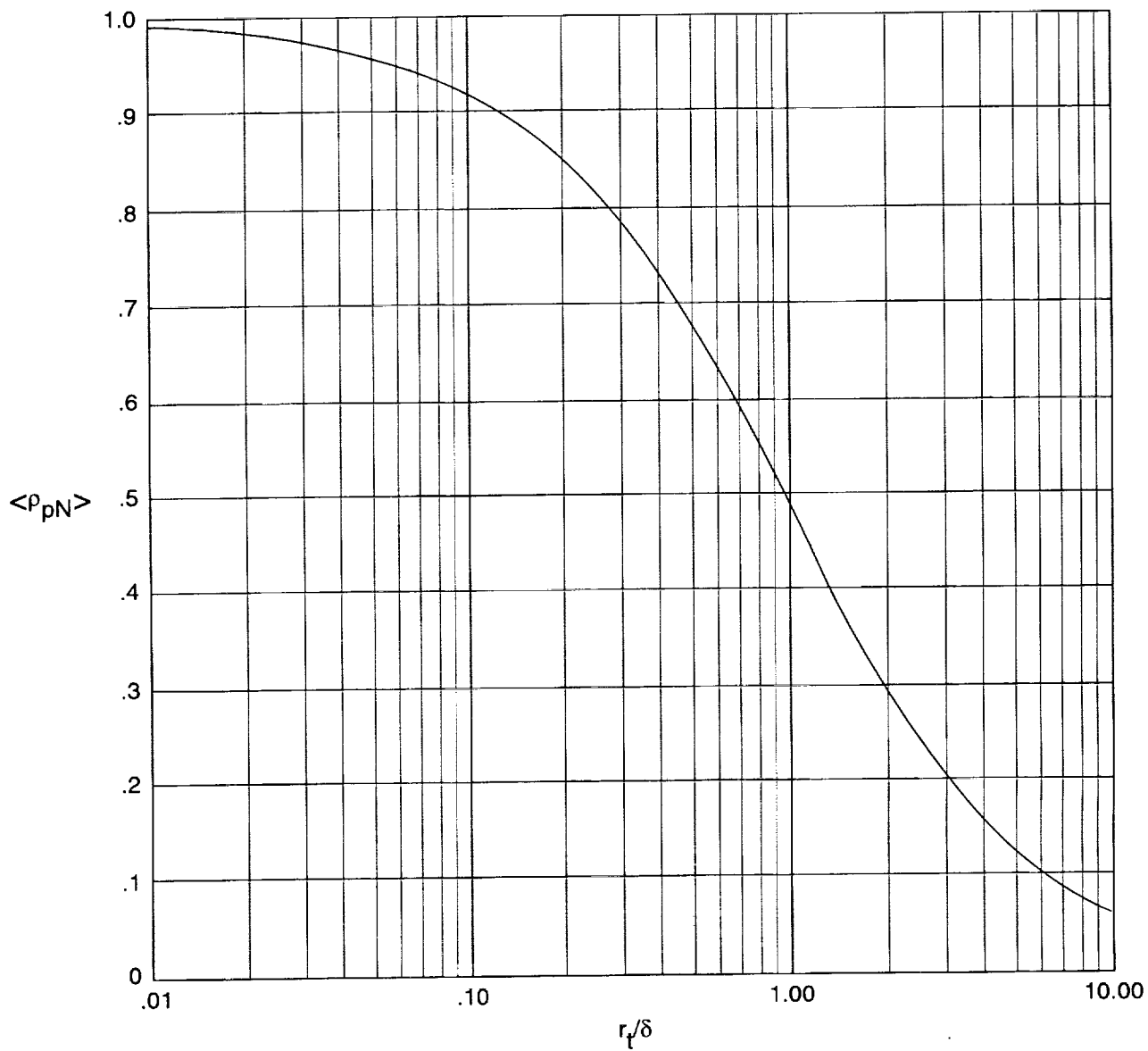Figure 22. Normalized pumping photon density ρ_{pN} versus normalized radius r_N for various values of r_t/δ.
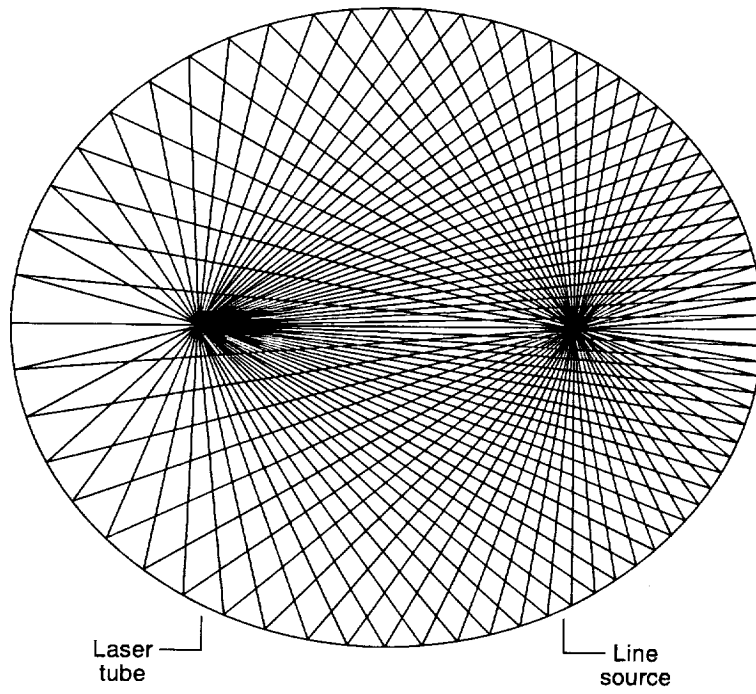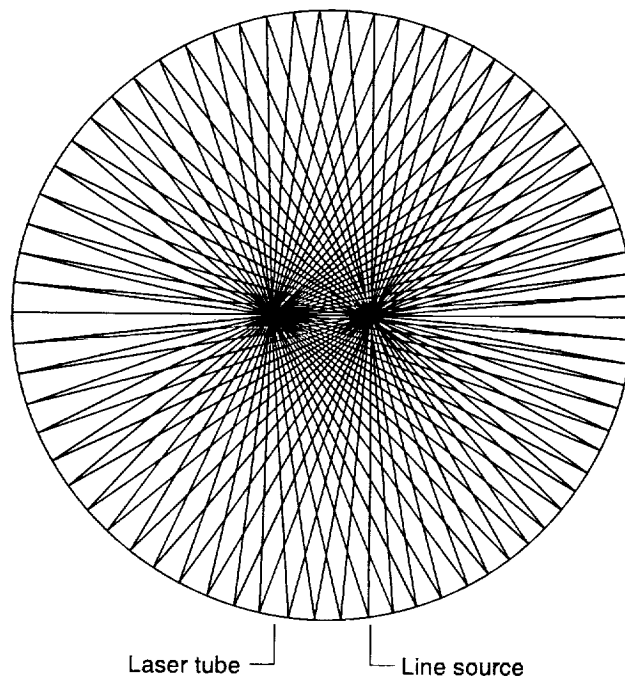
Figure 23. Normalized cross-sectional average pumping photon density $\langle \rho_{pN} \rangle$ versus r_t/δ.

(a) Elliptical section used in laser experiments.

(b) Elliptical section with closer focii.

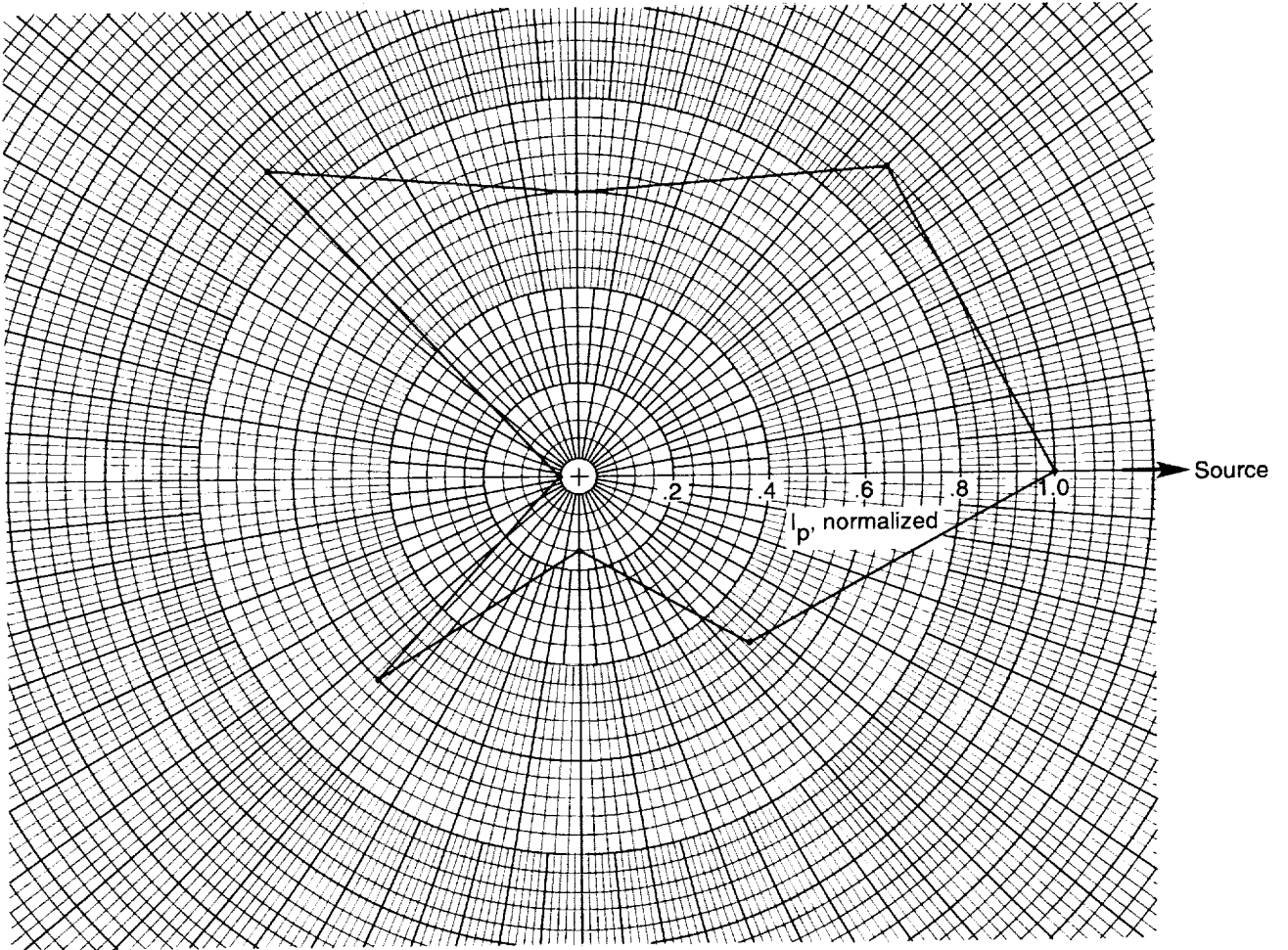Figure 24. Theoretical ray tracing for elliptical pump chamber with line source at right focus.

Figure 25. Polar plot of normalized incident pumping intensity I_p measured at inner radius of laser tube for elliptical pump chamber used in laser experiments. Corresponding theoretical ray tracing is shown in figure 24(a).

REPORT DOCUMENTATION PAGE

1. AGENCY USE ONLY *(Leave blank)*	2. REPORT DATE March 1995	3. REPORT TYPE AND DATES COVERED Technical Paper

4. TITLE AND SUBTITLE
Reduced Dimer Production in Solar-Simulator-Pumped Continuous Wave Iodine Lasers Based on Model Simulations and Scaling and Pumping Studies

5. FUNDING NUMBERS
WU 232-01-04-04

6. AUTHOR(S)
Robert C. Costen, John H. Heinbockel, Gilda A. Miner, Willard E. Meador, Jr., Bagher M. Tabibi, Ja H. Lee, and Michael D. Williams.

7. PERFORMING ORGANIZATION NAME(S) AND ADDRESS(ES)

NASA Langley Research Center
Hampton, VA 23681-0001

8. PERFORMING ORGANIZATION REPORT NUMBER

L-17391

9. SPONSORIING/MONITORING AGENCY NAME(S) AND ADDRESS(ES)

National Aeronautics and Space Administration
Washington, DC 20546-0001

10. SPONSORING/MONITORING AGENCY REPORT NUMBER

NASA TP-3486

11. SUPPLEMENTARY NOTES
Costen, Miner, Meador, Lee, and Williams: Langley Research Center, Hampton, VA; Heinbockel: Old Dominion University, Norfolk, VA; Tabibi: Hampton University, Hampton, VA.

12a. DISTRIBUTION/AVAILABILITY STATEMENT

Unclassified–Unlimited
Subject Category 36
Availability: NASA CASI (301) 621-0390

12b. DISTRIBUTION CODE

13. ABSTRACT *(Maximum 200 words)*

A numerical rate equation model for a continuous wave iodine laser with longitudinally flowing gaseous lasant is validated by approximating two experiments that compare the perfluoroalkyl iodine lasants $n\text{-}C_3F_7I$ and $t\text{-}C_4F_9I$. The salient feature of the simulations is that the production rate of the dimer $(C_4F_9)_2$ is reduced by one order of magnitude relative to the dimer $(C_3F_7)_2$. The model is then used to investigate the kinetic effects of this reduced dimer production—especially how it improves output power. Related parametric and scaling studies are also presented. When dimer production is reduced, more monomer radicals $(t\text{-}C_4F_9)$ are available to combine with iodine ions, thus enhancing depletion of the laser lower level and reducing buildup of the principal quencher, molecular iodine. Fewer iodine molecules result in fewer downward transitions from quenching and more transitions from stimulated emission of lasing photons. Enhanced depletion of the lower level reduces the absorption of lasing photons. The combined result is more lasing photons and proportionally increased output power.

14. SUBJECT TERMS
Continuous wave; Solar-simulator pumped; Iodine laser; Rate equation model

15. NUMBER OF PAGES
69

16. PRICE CODE
A04

17. SECURITY CLASSIFICATION OF REPORT Unclassified	18. SECURITY CLASSIFICATION OF THIS PAGE Unclassified	19. SECURITY CLASSIFICATION OF ABSTRACT Unclassified	20. LIMITATION OF ABSTRACT

National Aeronautics and
Space Administration
Langley Research Center
Mail Code 180
Hampton, VA 23681-0001